2009

In-Vitro Biocompatibility of Silver Nanoparticles Anchored on Multi-Walled Carbon Nanotubes

Alicia Brooks Castle
Wright State University

In-Vitro Biocompatibility of Silver Nanoparticles Anchored on Multi-Walled Carbon Nanotubes

A thesis submitted for the degree of Master of Science

By

Alicia B. Castle

B.A. Miami University

WRIGHT STATE UNIVERSITY
SCHOOL OF GRADUATE STUDIES

Date: May 14, 2009

I HEREBY RECOMMEND THAT THE THESIS PREPARED UNDER MY SUPERVISION BY ALICIA BROOKS CASTLE ENTITLED "*In Vitro* Biocompatibility of Silver Nanoparticles Anchored on Multi-Walled Carbon Nanotubes" BE ACCEPTED IN PARTIAL FULFILLMENT OF THE REQUIREMENTS FOR THE DEGREE OF Master of Science.

_____
Saber M. Hussain, Ph.D.
Thesis Advisor

_____
Terry Oroszi
Director, Grad Program

_____
Mariana Morris, Ph.D.
Department Chair

Committee on Final Examination:

_____
Courtney Sulentic, Ph.D.

_____
David R. Cool, Ph.D.

_____
Saber M. Hussain, Ph.D.

_____
Joseph F. Thomas Jr., Ph.D.
Dean, School of Graduate Studies

Abstract

Castle, Alicia M.S. Pharmacology and Toxicology, Wright State University 2009. *In Vitro* Biocompatibility of Silver Nanoparticles Anchored on Multi-Walled Carbon Nanotubes

Silver (Ag) nanoparticles were anchored on the surface of three different multi-walled carbon nanotubes (MWNTs): Ag-MWNTs (pure carbon), Ag-MWNT-COx (carbonyl and carboxyl doped), and Ag-MWNT-CNx (Nitrogen-doped). The chemical reactivity of the nanotubes was MWNTs< COx-MWNTs< CNx-MWNT. Ag-NP anchored on the MWNTs had an average size corresponding to MWNTs 6.64nm +/- 2.25nm; CNx-MWNTs, 13.24nm +/- 3.94nm, and COx-MWNT/Ag 11.75nm +/- 4.65nm. Cellular function and immune response were evaluated to determine biocompatibility of the synthesized nanomaterials (NM) on the human keratinocyte cell line (HaCaT). Cellular assays revealed toxicity after 24h however, full cellular recovery was observed at 48h. These results suggest Ag nanoparticles anchored on MWNTs have the ability to interact with cells without disrupting cellular function.

Table of Contents

List of Figures

List of Tables

LIST OF ABBREVIATIONS

µg	microgram
µl	microliter
Ag	silver
Ag-MWNT	multi-walled carbon nanotubes functionalized with silver
Ag-MWNT-CNx	nitrogen doped multi-walled carbon nanotubes functionalized with silver
Ag-MWNT-COx	carbonyl and carboxyl doped multi-walled carbon nanotubes functionalized with silver
Ag-NP	silver nanoparticle(s)
Al	aluminum
Al_2o_3	aluminum oxide nanoparticles
Al-NP	aluminum nanoparticle(s)
BRL-3A cells	immortalized rat liver cells
C18-4 cells	mouse germ line stem cells
FBS	fetal bovine serum
HaCaT	human keratinocyte cells
LDH	lactate dehydrogenase
mg	milligram
mL	milliliter
MMP	mitochondrial membrane potential
MTS	methyl tetrazolium
MTT	(3-(4,5-Dimethylthiazol-2-yl)-2,5-diphenyltetrazolium bromide)
MWNT	multi-walled carbon nanotubes
NM	nanomaterials
nm	nanometer
NP	nanoparticles
NT	nanotubes
NZVI	nanoscale zerovalent iron particles
PBS	phosphate buffered saline
PCR	polymerase chain reaction
PRB	permeable reactive barrier
ROS	reactive oxygen species
SD	standard deviation
STEM	
SWNT	single-walled carbon nanotubes
TBHP	tert-butyl hydrogen peroxide
TEM	transmission electron microscopy
XRD	X-ray diffraction

Acknowledgements

I would like to thank Col Riley, 711 HPW and Dr. John J. Schalger, RHPB Branch Chief. Throughout my thesis research work I was funded by the Consortium Research Fellows Program, to whom I owe a thank you to for their financial support. I would also like to thank my committee members, Dr. Sulentic and Dr. Cool for their help in preparing this thesis. Dr. Hussain, my advisor, who I could not have done this without. He has been a key factor in developing my scientific knowledge and I am very grateful to have been able to have him as a mentor. Thank you to Dr. Mauricio Terrones, Dr. Humberto Terrones, Edgar E. Gracia-Espino and Cesar Nieto-Delgado of the Advanced Materials Department and Laboratory for Nanoscience and Nanotechnology Research, IPICYT, for their help in making and characterizing the functionalized carbon nanotubes. I would also like to recognize the members of the Biological Interactions of Nanomaterials (BIN) group for their tireless help on my project. In particular I would like to thank Dr. Laura Braydich-Stolle for her continuous efforts on my project and acting as a second mentor to me.

In-Vitro Biocompatibility of Silver Nanoparticles Anchored on Multi-Walled Carbon Nanotubes

Background

Engineered nanomaterials (NM), in the range of 1-100nm in size (Fig. 1), possess novel physical and chemical properties that have been used or are proposed to be used to create unique devices. The distinctive quantum properties of nanomaterials strongly influence their physico-chemical properties, conferring electrical, optical and magnetic properties not present in their corresponding bulk counterparts[1,2]. Biological functionalization of nanomaterials has come to be of significant interest in the recent years due to the potential for developing sensitive imaging and signaling pathway detection systems[3] as well as possible drug delivery systems[4]. The biofunctionalization of nanomaterials' surfaces can result in aqueous soluble materials which can be further modified with active molecules making them compatible, active, specific capture field agents and useful in biological systems. While all of this seems promising it is still unknown how engineered nanomaterials of different size, structure, and geometries interact with cells and the molecular events involved in nanoparticle-membrane receptor binding, endocytosis and subsequent signaling activation.

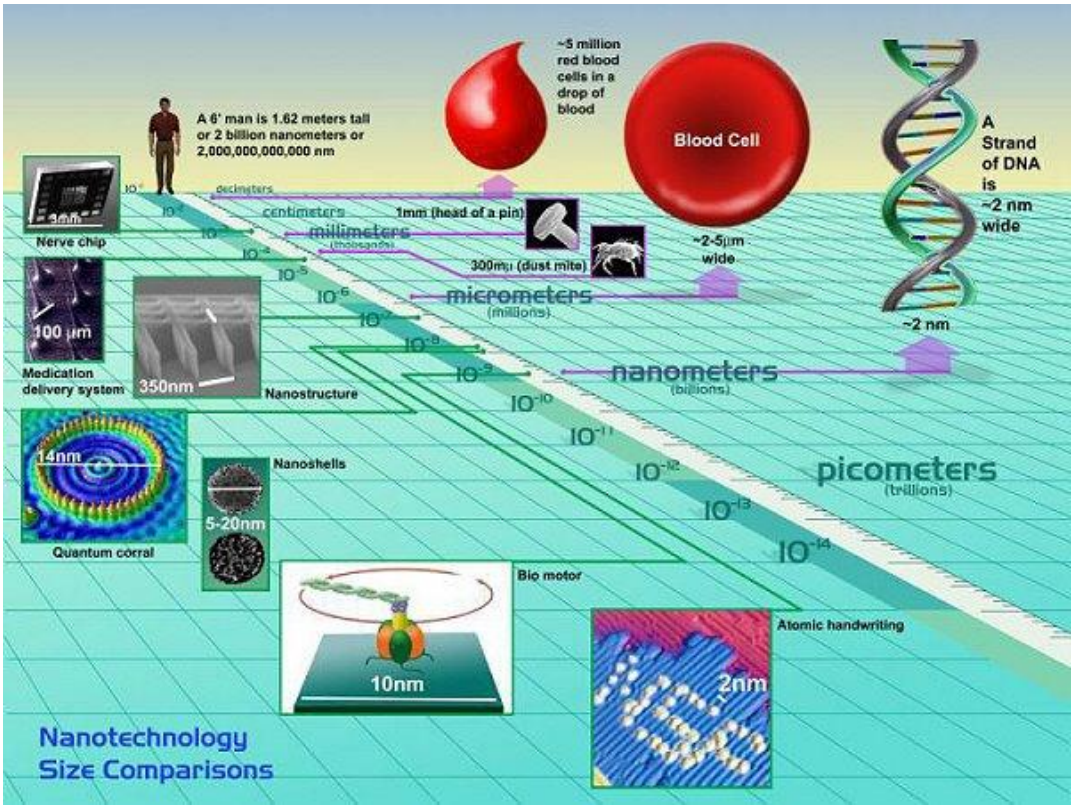

Fig. 1 Size comparison of Nanoparticles to household and scientific objects
http://www.terressentials.com/exposure.html

Nanosilver

Silver's (Ag) extremely small size and large surface area allow for different properties than the bulk material. Nano-silver possesses a high extinction coefficient, high surface plasmon resonance and anti-microbial properties which are less toxic then the bulk form[5,6]. In the future, nano-silver's high surface plasmon resonance has a possibility for many color based biosensor applications and different lab-on a chip sensors. The high surface plasmon resonance is beneficial for sensors, because silver has a typical excitation wavelength and when something disrupts the surface the excitation wavelength changes and we are able to detect what has been bound[7].

Currently silver nanomaterials have a variety of uses in everyday consumer's lives such as: nanosilver infused storage containers[8], nanosilver coated surfaces of medical devices to reduce hospital related infections[9], bandages[10], footwear[11] and countless household items which claim to be anti-microbial as shown in figure 2. Nanosilver is a popular additive in many health products as listed previously due to its unique ability to fight infectious diseases, slow the growth of bacterium, mold and germs. While all of these properties appear to make nanosilver the new "wonder-drug" of the nanotechnology world, problems arise.

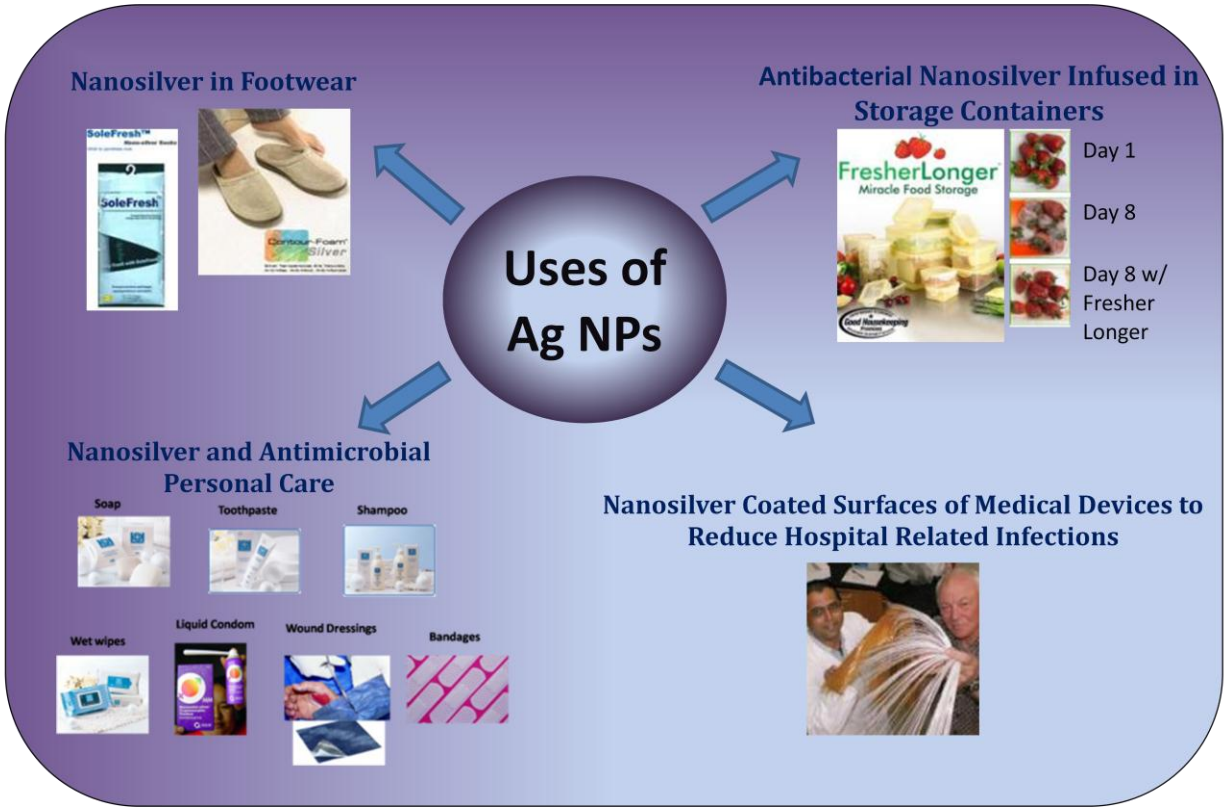

Figure 2. Medical and personal uses of silver nanoparticles.
Courtesy of Dr. Laura Braydich-Stolle

Nanosilver is Toxic in a Size dependent Manner

The problem with nanosilver is it has been shown to be toxic in a size dependent manner according to with reactive oxygen species (ROS) production shown to be the mechanism of toxicity[12]. In the treatment of rat alveolar macrophages, the toxicity is size and dose dependent with the most toxicity occurring with silver 15nm (Ag15nm) followed by silver 55nm (Ag55nm) and silver 130nm (Ag 130nm). It was also found that the smaller sizes of silver (Ag15-30nm) caused decreases in mitochondrial function and membrane integrity. A decrease in the membrane integrity allows the leakage of the ROS outside the cell leading to apoptosis[12]. Another possible mechanism of silver nanoparticle

toxicity is believed to be due to the strong affinity of silver to thiol groups (-SH)[13]. Thiol groups are the functional group of the amino acid cysteine and are considered highly reactive. Two thiol groups come together through an oxidation reaction causing a disulfide linkage, which is necessary for proteins to fold appropriately. If nanosilver interacts with the thiol groups, proteins are not able to form correctly and DNA can lose its ability to replicate[14].

In an effort to make the silver less toxic silver nanoparticles were coated with polysaccharide[15]. The polysaccharide coating is many monosaccharides or carbohydrates brought together with glycosidic bonds. Carbohydrates are a natural product in the body and therefore the polysaccharide coating itself does not produce toxicity. The polysaccharide coated particles show less agglomeration. The N2A (neuronal) cells were examined and showed greater reduction in viability in the Ag25 uncoated particles verses the Ag25 polysaccharide coated particles; therefore determining the coating reduces the toxicity of the Ag nanoparticles[15].

The coating seems like the answer, but overtime the coating dissolves in the body again rendering the cell to the toxic properties of the silver nanoparticles[16]. A study performed on germ line stem cells showed Ag-10-PS and Ag-15-HC caused the same decrease in cell viability after a three day exposure in neuronal cells. If the coating is dissolving after just three days in media, the time to toxicity could possibly be much quicker in the human body.

Functionalized Multi-Walled Carbon Nanotubes

In order to use the therapeutic properties of the silver nanoparticles they need to be determined non-toxic. One possible method for reducing the toxicity of silver nanoparticles is to functionalize them on multi-walled carbon nanotubes (MWNT). Multi-walled carbon nanotubes consist of multiple layers of graphite rolled on themselves forming a tube with a length to diameter ratio greater than 1,000,000. Figure 3 shows 2 models exist for MWNT the Russian Doll Model and the Parchment model. The Russian doll model consists of concentric graphite cylinders placed one inside of the next. The parchment model is a sheet of graphite rolled upon itself like a scroll.

Carbon nanotubes have many distinct properties such as strength 10-100 times greater than the strongest steel, but with a fraction of the weight due to sp^2 bonds throughout[17]. They also possess exceptional thermal and electrical properties making them useful for several devices such as field-emission displays[18], microscopy[19], microelectronics[20] and possibly drug delivery[4]. While they possess these exceptional characteristics figure 4 shows MWNTs also induce oxidative stress, granuloma formation, mesothelioma induction and genotoxic and mutagenic effects[21].

Multi-walled nanotubes have the possibility for use in drug delivery systems due to their chemical structure and unique ability to be functionalized. Functionalization of single walled nanotubes (SWCNT) leads to breakage of C=C bonds leaving holes in the structure causing changes in properties of the nanotubes. Unlike the SWCNTs, MWNTs do not have bond breakage and therefore there are no holes in the tube and they maintain their unique properties[22].

The multi-walled carbon nanotubes in this study have been doped with nitrogen or carbonyl groups and the functionalized with silver. Nitrogen and carbonyl groups were chosen to dope the nanotubes due to the fact that all living things contain nitrogen, carbon and oxygen. Nitrogen and carbonyl groups should lead to more biocompatibility since these groups are naturally occurring substances.

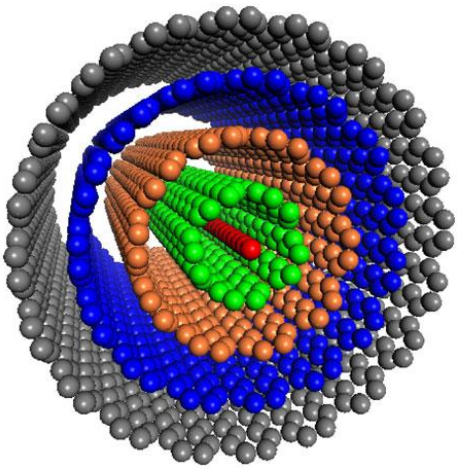

Figure 3. Depiction of Russian Doll Model of Multi-Walled Carbon Nanotubes
www.aip.org/png/2003/186.htm

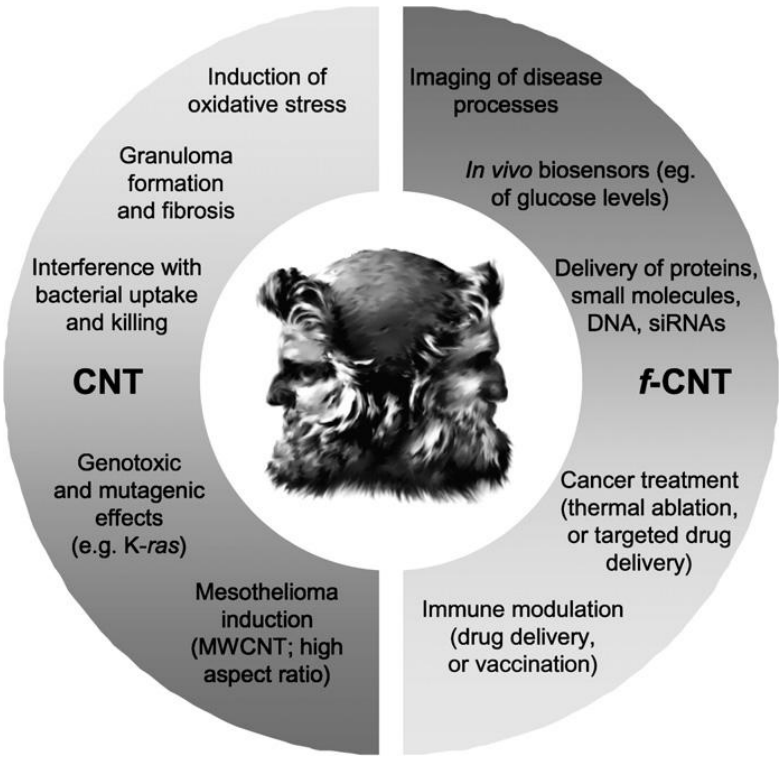

Figure 4. The Double sides of functionalized multi-walled carbon nanotubes. Multi-walled carbon nanotubes possess several methods which produce toxicity in cellular structures, but at the same time possess many opportunities in medicine.

Single/Multi-walled Carbon Nanotube Toxicity

Along with losing their chemical properties SWCNTs have shown toxicity in human keratinocytes (HaCaT cells)[23]. Upon exposure to the SWCNTs the HaCaT cells showed an increase in oxidative stress as well as morphological changes, which are attributed to the iron catalyst within the SWCNT. The response of the keratinocytes to the SWCNTs is similar to dermatological disorders including pigmentation changes, inflammation, prophyrias and some skin cancers and is often referred to as carbon fiber dermatitis[23].

When RAW 264.7 cells (macrophage-like, Abelson leukemia virus) have been exposed to MWNT asbestos-like toxicity was reported[24]. Multi-walled carbon nanotubes

have the possibility of entering the respiratory system when exposed to the nano-sized particles in a work environment. In a study by Poland et al, MWNTs produced asbestos like activity when injected into the abdominal cavity of mice[25]. The longer MWNTs produced more inflammation than the shorter MWNTs and caused the formation of foreign body giant cells and an increase in polymorphonuclear leukocytes. The response to the MWNTs in the abdomen was similar to the asbestos induced responses, because of the acute inflammatory response. The question still remains whether or not the inflammatory response will persist causing mesothelioma or if this will eventually normalize. If nanoparticles are able to enter the respiratory system they are also in contact with the largest organ, the skin. Therefore along with an exposure to the respiratory system these individuals will also have an exposure to their skin providing the support for accessing these nanotubes in human keratinocytes.

Information about the dermal toxicity of MWNTs is unknown and contradictory at this time. However, MWNTs have been shown to be biocompatible with neuronal cells. Astrocytes have the ability to bind to MWNTs leading to a reduction in scar tissue normally found with the implantation of neuronal devices[26]. Biocompatibility of MWNTs has also been show in osteoblasts. Osteoblasts have also been found to proliferate at higher rates on the nanotubes indicating a non-toxic possibility for bone regeneration[27].

A previous report about the toxicity of MWNTs in mouse keratinocytes by Grabinski et al. showed high levels of ROS production upon exposure to MWNTs[28]. The report also states the toxicity shown by the MWNTs is likely due to the iron impurities found in the MWNTs. Similar results were also found looking at MWNT and A549 cells *in* vitro. The A549 cells demonstrated a dose and time dependent increase in ROS

generation. When the MWNTs were treated with acid to remove the metal contaminates the study found the ROS generation did not occur[29]. Therefore pure MWNTs show promise for a biocompatible interaction with human keratinocytes.

MWNTs could be the answer to gaining the anti-microbial benefit of silver nanoparticles as well as future biosensor capabilities. As long as the functionalized multi-walled carbon nanotubes are in their purest state the nanotubes have a lower chance of producing toxicity and thus allowing the silver nanoparticles to enter the cells in a biocompatible manor. This study will determine if the functionalization of silver nanoparticles on multi-walled carbon nanotubes could be used in future drug delivery systems by delivering silver to the cell in a non-toxic, non-invasive method.

Human Keratinocytes

Skin is the largest organ of the human body and allows for sensations, thermoregulation, metabolic function and protection from both chemical and physical harm. A keratinocyte is the chief component of the epidermal layer of the skin, followed by melanocytes, Langerhans cells, and Merkels cells. Keratinocytes compose 95% of the epidermis and are one of the first things foreign objects come into contact with when an individual is exposed.

Figure 5 shows the Epidermis is composed of several layers based on the maturing keratinocytes. The Stratum Spinosum includes keratinocytes, which are changing to a polyhedral shape and producing tonofilaments. The outermost layer of the epidermis, the corneum granulosum, contains keratinocytes undergoing programmed cell

death[30]. Figure 6 shows images at 10x and 40 of the human keratinocytes used in this study under normal healthy conditions.

Immortalized human keratinocytes (HaCaT cells) are used as a cellular model to determine the interaction of nanoparticles with human skin. HaCaT cells produce cytokines such as interleukin (IL-1β), IL-6, IL-8, interferon IFN-γ, granulocyte-colony stimulating factor (G-CSF), macrophage inflammatory protein (MIP)-1β, and tumor necrosis factor-alpha (TNF-α)[31]. Increases in these cytokines can lead to an inflammatory response, which can be measured using real time PCR. Specifically increases in TNF-α can activate the NF-κB pathway and result in transcription of genes involved in stress and inflammation. NF-κB can lead to apoptosis or cellular recovery[32].

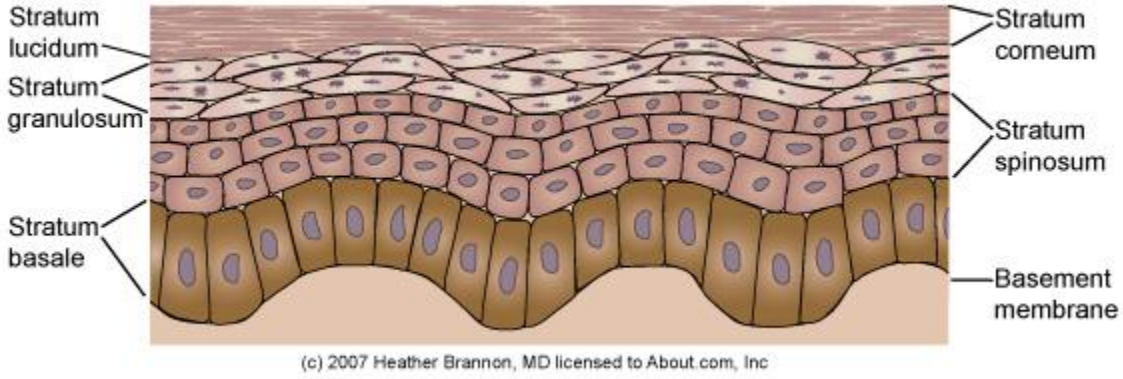

Figure 5. Schematic representing the layers of the epidermis, which is composed of 95% keratinocytes.
http://z.about.com/d/dermatology/1/0/e/4/Epidermis_Full_lucid.jpg

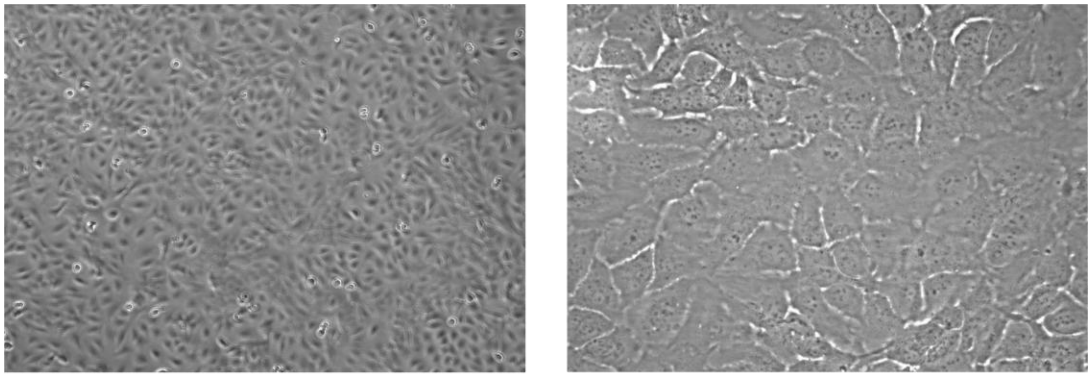

10X Image of HaCaT cells. 40X Image of HaCaT cells.

Figure 6. Microscope images of Human Keratinocytes at 10X and 40X

Purpose

In this study the biocompatibility of multi-walled carbon nanotubes functionalized with silver will be examined. One set of multi-walled carbon nanotubes will be doped with nitrogen and another set was doped with carbonyl groups before being functionalized with silver in an attempt to make the nanotubes more biocompatible. The endpoints to examine toxicity will show cellular integrity, mitochondrial integrity and inflammatory response produced by the nanotubes.

Previous work with multi-walled carbon nanotubes has shown their toxicity could be due to reactive oxygen species generation thus causing an inflammatory response of the cells[28]. Therefore, ROS generation will be examined and the inflammatory response of the human keratinocytes will be measured. Human keratinocytes have been shown to secrete IL-6 and TNF-α during times of cellular stress[31], so these inflammatory cytokines will be measured as an endpoint of toxicity.

Functionalized nanomaterials have great possibilities for use in imaging of disease processes, *in vivo* biosensors, as delivery vehicles for small proteins, cancer treatment or drug delivery systems. Multi-walled carbon nanotubes have been shown to induce granuloma formation, induce mesothelioma and cause genotoxic and mutagenic effects. These toxic effects could possibly be mediated by using different purification methods and different particles for functionalization allowing for the benefits of the carbon nanotubes.

The purpose of this study will be to determine the whether multi-walled carbon nanotubes functionalized with silver cause a toxic reaction to the human keratinocytes or if they are biocompatible. The second phase of the study will look at the ability of the human keratinocytes to recover after an acute exposure to the nanotubes. If there is no

toxicity after an acute exposure there will be no recovery, but if there is toxicity time to recovery will be determined. Time to recovery will show if it will be possible to use these nanotubes as a drug delivery system for a one time dose or if even one exposure is too harmful. This study will provide imperative information on the interaction between human keratinocytes and multi-walled carbon nanotubes and our next steps in gaining scientific use of the nanotubes.

Hypothesis

Silver nanoparticles have potential in drug delivery systems due to their anti-microbial properties. If silver nanoparticles produce toxicity in human systems, their future applications in drug delivery will not be possible. It can be hypothesized multi-walled carbon nanotubes will reduce the toxicity of silver nanoparticle and thus allow them to be used as anti-microbials and biosensors.

Specific Aims

Specific Aim 1: Characterize the 3 MWNT-Ag composites to determine if the nanotubes and particles are the correct size and if there is any agglomeration.

Specific Aim 2: Examine the production of reactive oxygen species and inflammatory genes activated/deactivated by the MWNT-Ag composites.

Specific Aim 3: Examine the cellular recovery of the HaCaT cells exposed to carbon nanotubes in cell viability assays such as MTS.

Experimental Design

Nanotube Synthesis

Three types of multiwalled carbon nanotubes (MWNTs) were prepared. The nanotubes were synthesized using a chemical vapor deposition (CVD) method. The pure MWNTs were synthesized by the thermal decomposition of a mixture of 2.5%wt of ferrocene ($FeCp_2$; 98% Aldrich®) and toluene (C_7H_8; 99.9% Fermont®) at 825°C in an Ar atmosphere for 30 min, follwing the method described elsewhere[33]. Similarly, Nitrogen-doped multiwalled carbon nanotubes (CNx-MWNTs) were obtained by decomposition of a solution containing 2.5%wt of ferrocene and benzylamine (C_7H_9N; 99% Sigma-Aldrich®). Finally, ethanol-based (carbonyl and carboxyl functionalized) carbon nanotubes (COx-MWNTs) were produced using a solution of ferrocene (2.5%wt), 1%wt of ethanol (CTR scientific®) and toluene (C_7H_8)[34].

Ag Anchoring on MWNTs: The three different types of nanotubes tested in this work were used without any chemical modification (e.g. water or acid treatments). The general procedure consisted of adding 1mg of the nanotubes to a solution of acetone (C_3H_6O; 20 ml) and silver nitrate ($AgNO_3$; 83µl from a solution 0.1 N, J.T. Baker®) in a flask. Subsequently, the suspension was dispersed ultrasonically for one hour. The solution was then placed in a water bath to increase the temperature to 60°C, and at this point 10 ml of N,N-dimethylformamide (DMF, 99% Sigma-Aldrich®) was added as a reducing agent; the temperature of the suspension was maintained for 20 additional minutes. Subsequently, the nanotube samples were centrifuged, washed with distilled water twice and dried at 70° C in an oven.

Materials Characterization

The characterization of the composites were carried out by scanning electron microscopy (FEG-SEM, FEI XL30 FEG/SFEG) operated at 15 kV. The X-ray powder diffraction pattern of all samples were performed using a XRD D8 ADVANCE – BRUKER AXS, with a Cu K_α radiation (λ = 1.54060 Å). The operating current and voltage were maintained at 35 kV and 25 mA. High resolution images were taken with a HRTEM -field emission JEOL-JEM-3000F operating at 300 keV.

Human Keratinocytes (HaCaT cells)

HaCaT cells were donated generously by Dr. James F. Dillman III, of the U.S. Army Medical Research Institute of Chemical Defense 3100 Ricketts Point Rd Aberdeen Proving Ground, MD 21010-5400. The HaCaT cells maintained in RPMI-1640 with 1% Penicillin-Streptomycin and 10% FBS at 37.0°C and 5% CO_2[51]. The cells were passaged using Trypsin-EDTA and PBS when they reached 70-80% confluency. For nanomaterials exposures, RPMI media supplemented with 1% penicillin/streptomycin was used.

Reactive Oxygen Species Generation

In an attempt to measure the ROS production the DCFDA probe was used, which fluoresces green when ROS is present. The cells were plated at 50,000cells per well in a 96 well black synergy image plate. Cells were then treated with 25µg/mL nanomaterials for 24h. The positive control was 100µl of tert-Butyl hydroperoxide (TBHP). After 24h the cells were washed three times with PBS and stained with the DCFDA probe and hoescht. The Hoescht stain was used as a nuclear counterstain. The plate was examined

using the confocal microscope and it was qualitatively determined if there was ROS production versus the control. The MWNTs were doped with nitrogen and carbonyl groups leading to results that could not be considered accurate for ROS production since the probe could react with the oxygen and nitrogen on the functional groups.

Mitochondrial Membrane Potential

The mitochondrial membrane potential was measured to examine changes in the mitochondrial membrane, which correlates to ROS production and apoptosis.

HaCaT cells were plated at 80-90% confluency in 96 well black synergy image plates. The cells were dosed with 25µg/mL of nanomaterials for 24h. The Mit-E-Ψ Mitochondrial Permeability Detection Kit (AK-116) was used throughout the assay. To make the stain 125µL DMSO was added to the bottle of Mit-E-Ψ included in the kit. I added Hoescht stain to the Mit-E-Ψ stain at a 1:1000 concentration. A 1X buffer was made from the 10X buffer using sterile water at 34 °C. After 24h the cells were washed with 1xPBS and 100µL of stain was added to the cells for 15mins at 37°C. After 15mins the cells were washed twice with the 1x buffer made previously and placed in 100µL of 1x buffer for imaging. The cells were imaged using the confocol microscope and MMP was measured based on images and computer software, which compares the fluorescent intensity of each well to the control.

Inflammatory Response

The inflammatory response of the HaCaT cells exposed to nanotubes was measured using real-time PCR. HaCaT cells typically produce IL-6 and TNF-α, so these cytokines were chosen to be measured[31].IL-6 and TNF-α primers were ordered from Integrated DNA technology (IDT) and used for PCR.

Cells were plated at 300,000 cells/mL in 6 well plates and dosed with 25µg/mL of the different nanomaterials for 6h and 24h. After each time point the RNA was isolated using the Qiagen RNA isolation kit. The isolated RNA was then NanoDropped to determine the amount of RNA present in the sample. Then 1µg of RNA was used in real time PCR analysis. The Express Script from Invitrogen was used and 100nM forward and reverse primers for TNF-α, IL-6 and beta actin were used. On the Stratagen MX3005P the RNA was reverse transcribed for 30min at 50°C and then amplified using a cycle of 94°C for 30sec, 60°C for 1 min at 40 cycles. The TNF-α, IL-6 expression was normalized based on beta actin expression.

Cellular recovery

CytoViva

CytoViva imaging was used to determine the interaction between the particles and the cells[34]. Initial images were obtained using the transmitted light of the microscope to determine the initial cellular structure and the structure of the cells after 24h of exposure. Human Keratinocytes were plated at a cell density of 300,000cells/mL and dosed with 25µg/mL concentrations of nanomaterials in exposure media for 24 hours. At 24 h the

cells were washed 3x with 1xPBS and a coverslip was placed on the slide for live cell imaging on the CytoViva microscope.

HaCaT cells were plated in 2 chambered slides at cell densities of 300,000cells/mL and incubated for 24 hours. After 24 hours the cells were dosed with 25µg/mL concentrations of nanomaterials in exposure media for 24 hours. The cells were fixed in 2% paraformaldehyde and imaged using the CytoViva microscope. The HaCaT were then rinsed once with PBS and stained using the AlexaFluor 555-Phallodin actin stain. They were then stained with 25µL of stain per mL of media and incubated at 37°C. 1-2 drops of antifade with DAPI were added to each chambered.

Cell viability

Cell viability was assayed by MTS as indicated by the CellTiter 96®AQueous One Solution from Promega, which measures mitochondrial function and directly correlates to cell viability. The relative cell viability (%) related to control wells containing cell culture exposure media without nanoparticles was calculated by [A]test / [A] control x 100, where [A]test is the absorbance of the test sample and [A]control is the absorbance of control sample. Each experiment was done in triplicate.

Results

Characterization

The MWNT tubes differed in chemical reactivity when carrying out ouir thermogravimetric analysis, in which CNx-MWNTs were the most reactive and oxidized faster than MWNTs and COx-MWNTs. Therefore the reactivity observed can be summarized as follows: MWNTs < COx-MWNTs < CNx-MWNTs. Figure 1 shows STEM images of the Ag-MWNTs composites and their particle size distribution. The Ag-MWNTs composite is presented in Figure 7-(**a-c**) with an average particle size of 6.64 ± 2.25 nm. Figure 7-(**d-f**) shows the COx-MWNTs-Ag, and this composite presented a bimodal histogram in the Ag particle size, the first peak at ~8 nm and the second one at ~12 nm with an average size of 11.75 ± 4.65 nm. Finally, Figure 7-(**g-i**) shows the CNx-MWNTs-Ag composite, this material also exhibited a bimodal behavior in the Ag particle size (~10 and ~ 13 nm), giving an average value of 13.25 ± 3.94 nm. Figure 8 shows the X-ray powder diffraction patterns of the three Ag-nanotube systems, the G(002) peak corresponded to graphite, the others belonged to Ag nanoparticles; Ag planes are indexed and the materials revealed a high degree of crystallinity. Figure 9 reveals the TEM and HRTEM images of the Ag-MWNT system, showing the excellent anchoring of Ag nanoparticles on the tube surface. HRTEM images of the particles reveal a highly crystalline material that is well bonded to the tube surface.

Mitochondrial Membrane Potential

Measuring the mitochondrial membrane potential at 24h after exposure showed a significant decrease in mitochondrial membrane potential (Figure 10A). The significant

decrease in MMP indicated a decrease in cell viability. The decreases in MMP provide information that the cell is undergoing oxidative stress and possibly preparing to undergo apoptosis. Pictures taken with the confocal microscope showed the same qualitative results. The pictures showed more red fluorescence in the CNx-MWNT-Ag and COx-MWNT than the control (Figure 10B), and also slightly more red fluorescence in the MWNT-Ag, indicating a reduction in mitochondrial membrane potential (Figure 10B). Control Cells showed no red fluorescence, while the positive controls showed high amounts of red fluorescence indicating that the test was adequately performed (Figure 10). Mitochondrial membrane potential measures the amount of hydrogen ions pumped across the inner mitochondrial membrane during oxidative phosphorylation and the change in the amount of hydrogen pumped out is measured and related as the mitochondrial membrane potential. A decrease in the mitochondrial membrane potential also leads to the conclusion that the cells are responding to an oxidative stress.

Inflammatory Response Genes

Changes in inflammatory response can provide incite in the cellular environment and determine cellular stress. Figure 11 shows the PCR results at 6h, and illustrated slight increases in TNF-α and IL-6 when compared to the control. The MWNT-Ag, CNx-MWNT-Ag and COx-MWNT-Ag all showed a small initial increase in IL-6 and TNF-α, but it was not considered significant. After 24h, the increase in IL-6 did not change in any of the treatment groups, but TNF-α continued to increase (Figure 11) in the MWNT-Ag and COx-Ag. This could be due to IL-6 stimulating the immune response of TNF-α, thus leading to inflammation. The increase in TNF-α could activate the NF-κB pathway

and result in transcription of genes involved in stress and inflammation. NF-κB can lead to apoptosis or cellular recover and due to recovery assays we performed we can hypothesize the cells are recovering[32].

Cell Morphology

Initial images of the cells and particles without stain using visible light are depicted in figure 12 and showed the particles were interacting with the cells, but there was no change in cellular morphology when they were compared to the control.

Figure 13 shows all three types of MWNTs coated with Ag entered the cells, and were bound to the nucleus or nuclear region based on the CytoViva imaging. We could also determine the binding due to the high concentration of MWNTs in the images taken after 1 week. The cells had been washed and placed in exposure media for a week. The human keratinocytes appeared to exhibit some actin filament disruption caused by the Ag-MWNTs. However, the MTS results showed no toxicity, but rather an increase in cell viability. Some of the actin filament disruption could be due to the exposure media, because the cells do not grow normally due to the lack of FBS. This is also indicated in the control cells, which appear to become rounded over time. The ability of human keratinocytes to recover after an acute exposure demonstrates these Ag-nanotube systems still have a possibility for being used as delivery systems even, with an initial toxicity.

MTS

Figure 14 shows the MTS results of the HaCaT cells exposed to varying concentrations of Ag-nanotubes. The cells have completely recovered from the exposure by the 48h timepoint. (Figure 14). The decreases in cellular viability observed after 72h and 1 week could be caused by the cells having a large increase in viability at 48h and becoming over confluent, thus causing cell death. Cell viability could also have decreased due to the cells being placed in the exposure media, which does not contain the FBS needed for normal cellular growth. Table 2 shows the summary of the acute exposure to the nanomaterial composites.

Discussion

MWNTs have a potential use as an imaging agent or as a biosensor. Due to their near infrared emission they are able to respond to local dielectric function but still remain stable[35]. MWNTs also have the ability to be doped with different functional groups providing more hope for their future use in these fields. Detection using MWNTs would allow us greater tissue penetration and reduce fluorescent background. Imaging would last for under 24h and therefore would be considered an acute exposure. Based on our results, we would expect to observe an immediate inflammatory response, but the body could recover from this exposure. With the cells being able to recover, this technique could be used in future imaging procedures. It is also important to mention that these Ag-tube systems do not contain any thiol groups, and further studies with Ag nanoparticles

with thiol groups should be carried out. Our study examined the biocompatibility of MWNTs coated with Ag nanoparticles, a known anti-microbial agent, and doped with nitrogen and carbonyl groups to increase the biocompatibility.

The functionalized MWNTs used in this study produce an inflammatory response at 6h and at 24h indicating toxicity. At 6h IL-6 and TNF-α were both relatively low, but TNF-α continued to increase at the 24h time point, suggesting IL-6 promotion of TNF-α. Because TNF-α activates several other inflammatory pathways such as NF-κB can assume The increase in TNF-α could activate the NF-κB pathway and result in transcription of genes involved in stress and inflammation. NF-κB can lead to apoptosis or cellular recover and due to recovery assays we performed we can hypothesize the cells are recovering[32].

Mitochondrial membrane potential measures the amount of hydrogen ions pumped across the inner mitochondrial membrane during oxidative phosphorylation and the change in the amount of hydrogen pumped out is measured and related as the mitochondrial membrane potential. A decrease in the mitochondrial membrane potential leads to the conclusion that the cells are responding to an oxidative stress, but it can be assumed the oxidative stress is not strong enough to push them into apoptosis due to cellular recovery assays we performed.

While the cells show this initial inflammatory response, we observe that they also have an ability to recover over time. The inflammatory response must help the cells to recover from the exposure rather than send the cells directly into apoptosis. The results of the MTS a 24h, 48h, 72h and 1 week reveal that the cells show an increase in viability over time and thus the cells are recovering. The recovery period occurs in as little as 48h

for each of the exposures. After the 48h time point we do observe a decrease in cellular viability, but this is not believed to be due to the presence of the nanomaterials. This is possibly due to the cells becoming too confluent in the 96 well plate, and being in the exposure media for long periods of time.

CytoViva images also reveal that the cells have an ability to recover from the acute exposure to the Ag-nanotubes. The images show the Ag-nanotubes are binding to the cells, but there is little actin filament disruption and the nucleus is still intact. The human keratinocytes were washed after 24h, and allowed to recover in exposure media for up to a week. The ability of human keratinocytes to recover after an acute exposure demonstrates these Ag-nan0tube systems still have a possibility for being used as a drug delivery systems even, with an initial toxicity.

Ag nanoparticles have been shown to be toxic in a size dependent manner. In particular Ag-15 has been demonstrated to be toxic to immortalized liver cells (BRL-3A) and rat alveolar macrophages (C18-4). Ag-15 has been shown to be toxic regardless of the coating, which was in agreement with the results that Ag toxicity increases with size reduction[15,16]. Silver is the most toxic at small sizes due to its ability to produce more ROS at the smaller sizes[12]. The Ag nanoparticles used in this study were all under 30nm and should have been toxic in a size and dose dependent manner. When comparing ROS production and cell viability between previous studies and our study at the same concentrations and time points, we observed a much greater increase in biocompatibility for the Ag nanoparticle anchored on any type of MWNTs rather than isolated Ag nanoparticles.

All three carbon nanotubes were coated with Ag, but interestingly those Ag systems containing the CNx-MWNTs and COx-MWNTs did not increase biocompatibility. MWNTs with nitrogen and carbonyl groups produced a greater reduction in mitochondrial membrane potential versus the pure carbon MWNTs (CNx>COx>MWNT). Nitrogen and the oxygen from the carbonyl group could be forming ROS products within the cell. The functional groups could also be interacting with proteins or cell structures. These interactions could lead to the inhibition of cellular processes causing the reduction in cell viability. While they do cause the reduction in mitochondrial membrane potential, the presence of MWNTs first creates an inflammatory response to protect cells, but then they are responsible for repairing the human keratinocytes.

In a study performed by Cheng et al., the acute and long term effects of functionalized MWNTs were examined in zebrafish. In the early stages, the zebrafish generated an immune response[36]. The zebrafish that were exposed to the MWNTs produced an initial response, but the nanotubes were cleared from their body after 96h. However, the second generation of the zebrafish had lower survival rate suggesting that MWNTs had no significant toxicity initially but did display long term effects on the progeny[36]. These results agree with ours showing a significant inflammatory response followed by the cells capacity for recovery, long term exposures need to be examined in the future.

Nanomaterials hold the key to several unopened doors in the science field, but several questions still need to be answered. Is the possibility of a toxic reaction worth the risk? Further biocompatibility assays need to be performed before Ag-nanotube systems

can be considered for medical or biological uses. If we can functionalize carbon nanotubes to be biocompatible the possibilities are endless.

A

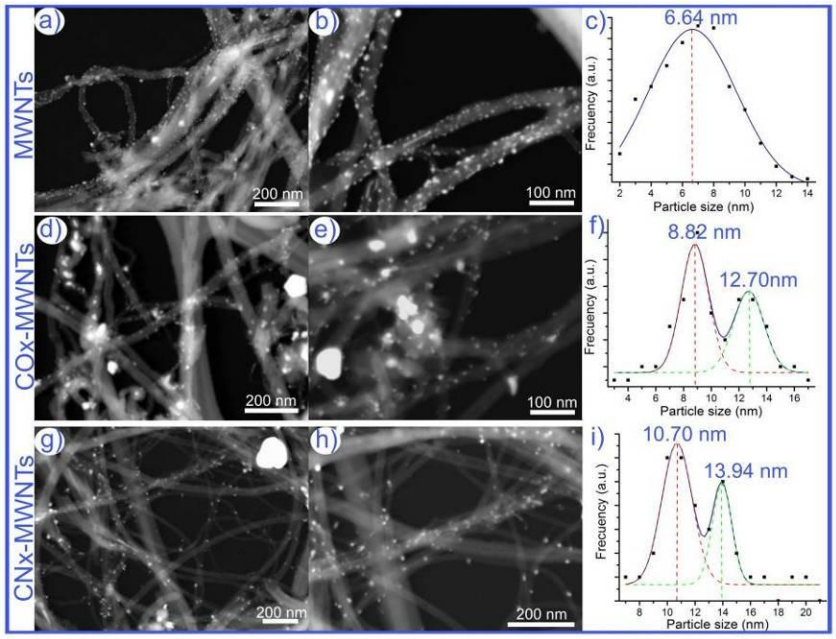

Figure 7. STEM images of **(a,b)-** MWNT, **(d,e)** COx-MWNTs and **(g,h)** CNx-MWNT. The particle size for each particle type are included as follows (**c)** MWNT 6.64nm, **(f)** Cox-MWNT 8.82nm and 12.70nm and **(i)** CNx-MWNT 10.70nm and 13.94nm

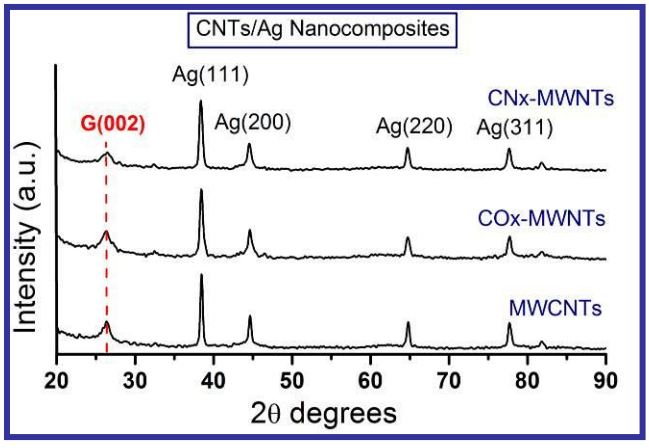

Figure 8 X-ray diffraction patterns of Ag-MWNT composites showing the expected graphite peak at ~26 2Θ degrees and the different faces of the silver along the Nanotubes (Ag 111, Ag 200, Ag220, and Ag311).

Table 1.-The different sizes of two crystalline faces of Ag particles (Ag 111 and Ag 200) on the MWNT composites. Each nanotube has silver particles anchored on it, which are under 30nm.

Nanotubes	Ag(111) nm	Ag(200) nm
MWNT	27.94	27.78
COx-MWNTs	19.50	27.87
CNx-MWNTs	19.97	21.13

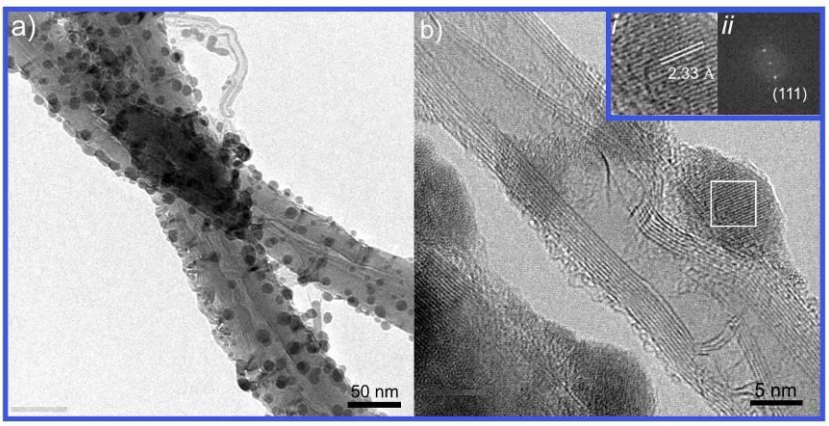

Figure 9. - TEM image of Ag-MWNT. (**a**) shows the high number of nanoparticles anchored on the nanotube's wall. (**b**) Higher magnification of the Ag-MWNT composite, the inset illustrates a magnification of Ag nanoparticle and their Fast Fourier Transform (FFT) showing the Ag (111) plane

a.

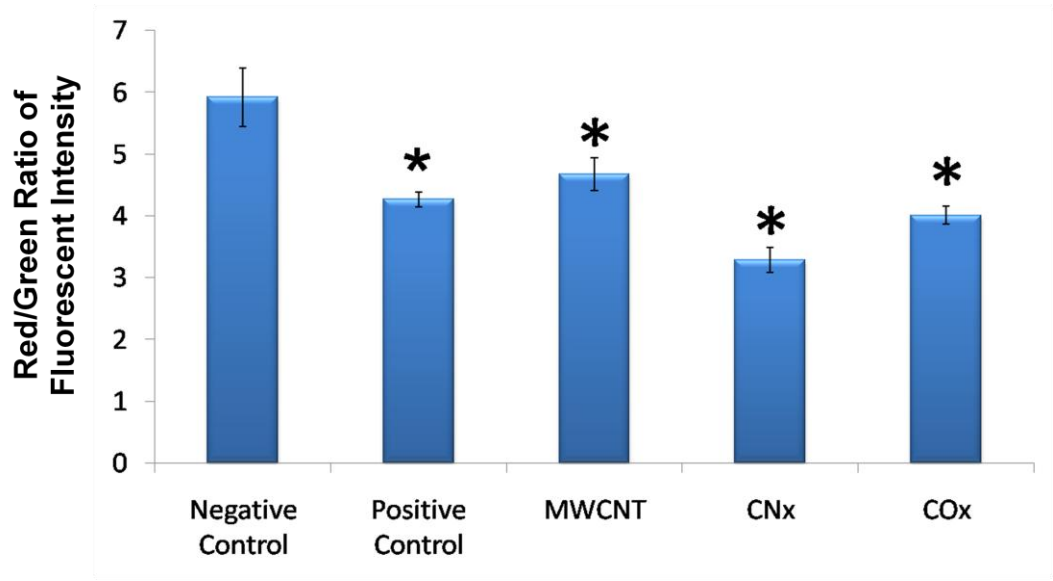

b.

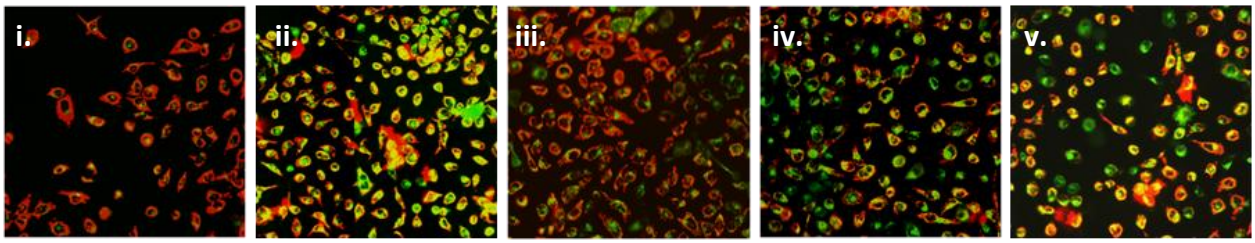

Figure 10. Reduction in Mitochondrial Membrane potential (MMP) after 24h of exposure to 25µg/mL of Ag-MWNT composites. **(a)** shows the fluorescent intensity measurements of cells treated with Ag-MWNTs verses untreated HaCaT cells. The decreases in the ratio corresponds to a decrease in MMP. An * shows a significant decrease. **(b)** Shows qualitative confocal images of HaCaT cells **(i)** control, **(ii)** positive control **(iii)** Ag-MWNT, **(iv)** Ag-MWNT-CNx, **(v)** Ag-MWNT-COx.

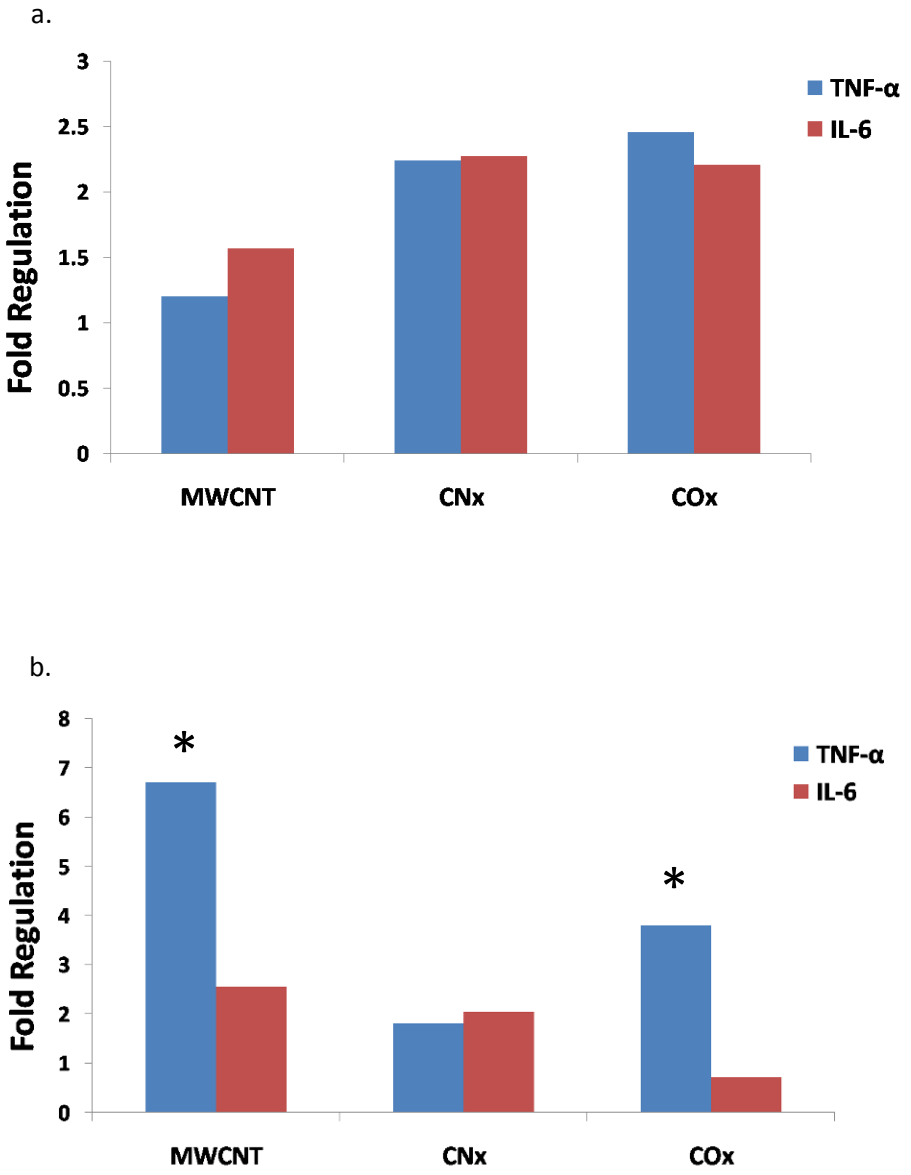

Figure 11. Change in inflammatory cytokine expression following **(a)** 6h and **(b)** 24h exposure to nanomaterials. Real Time PCR results show fold changes in the inflammatory markers TNF-α and IL-6. We do not see any significant increases at 6h, but significant increases in TNF-α are shown for cells treated with Ag-MWNT and Ag-MWNT-COx for 24h.

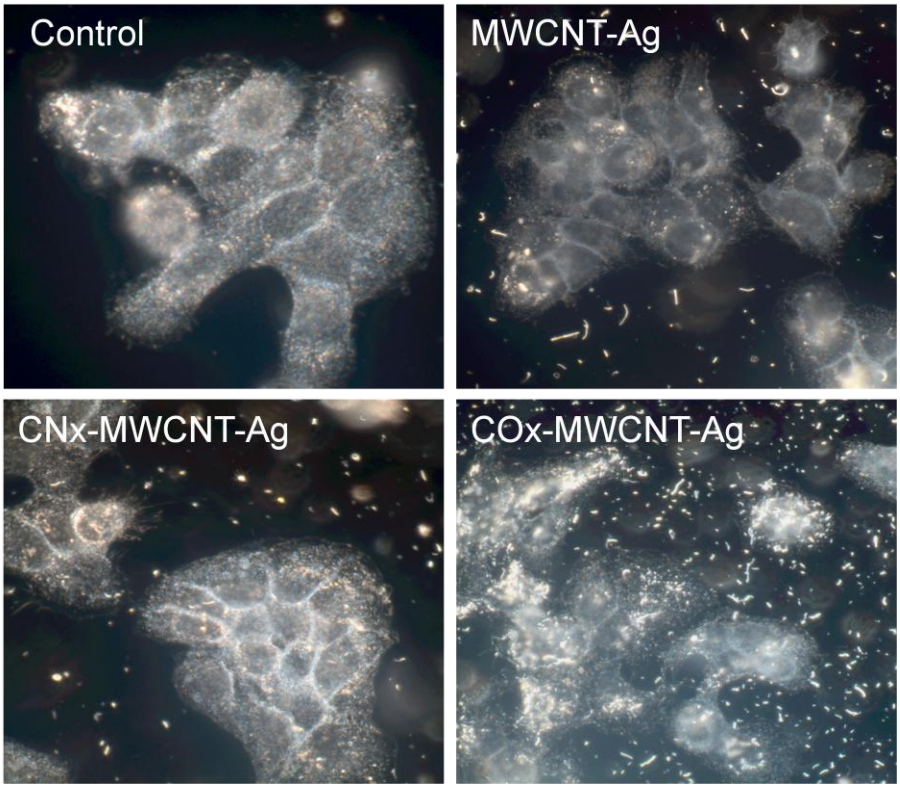

Figure 12. Live Cell CytoViva images of Human Keratinocytes exposed to 25µg/mL of nanomaterials for 24h.

CytoViva

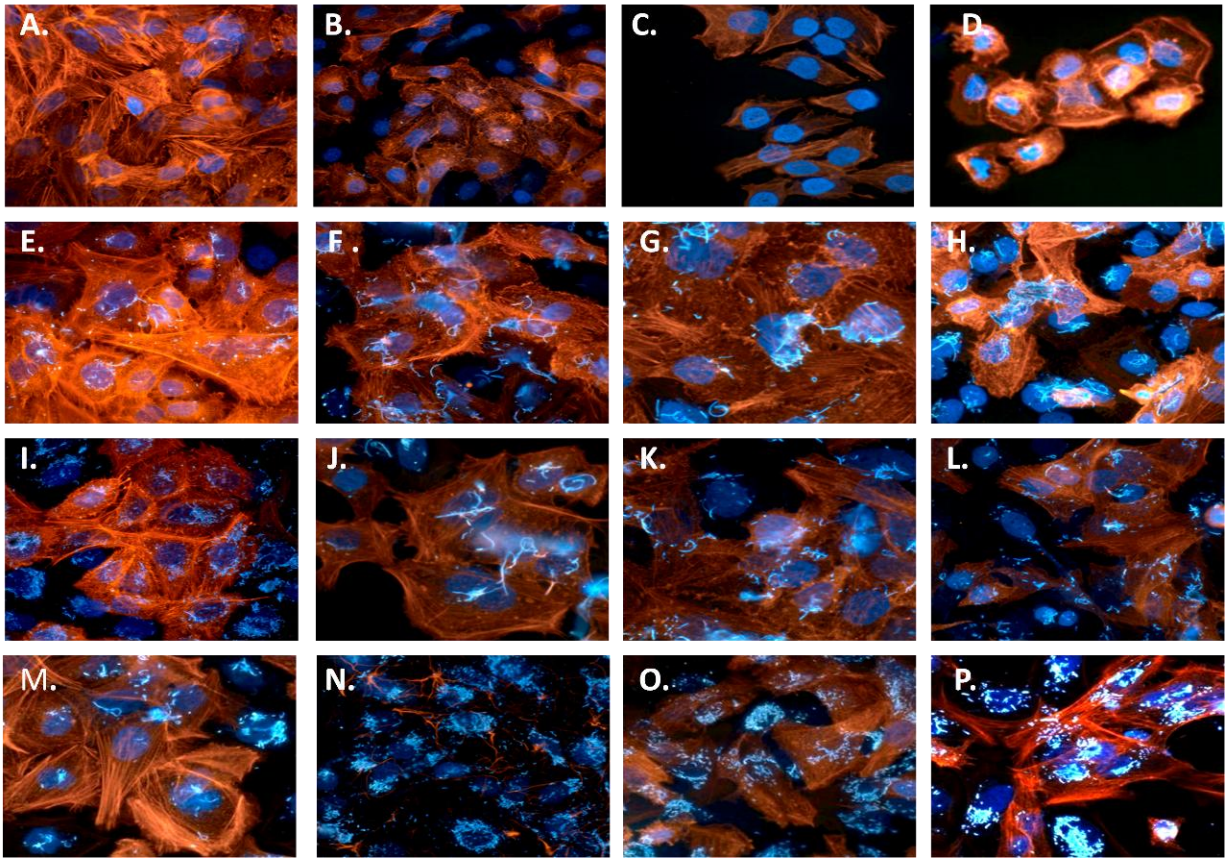

Figure 13. CytoViva imaging of HaCaT cells dosed with nanomaterials and then stained for actin Control HaCaT cells at **(A)** 24h, **(B)** 48h, **(C)** 72h and **(D)** 1 week. Ag-MWNTs at **(E)** 24h, **(F)** 48h, **(G)** 72h and **(H)** 1 week. Ag-CNx at **(I)** 24h, **(J)** 48h, **(K)** 72h and **(L)** 1 week and Ag-COx **(M)** 24h, **(N)** 48h, **(O)** 72h and **(P)** 1 week. Each picture with the MWNTcomposites shows localized nuclear binding with the nucleus stained blue and the actin filaments stained red/orange. The particles appear as the bright spots. There appears to be limited actin filament disruption in comparison to the control pictures. Binding can be determined based on the number of particles seen even after the 1 week time period in the exposure media.

a.

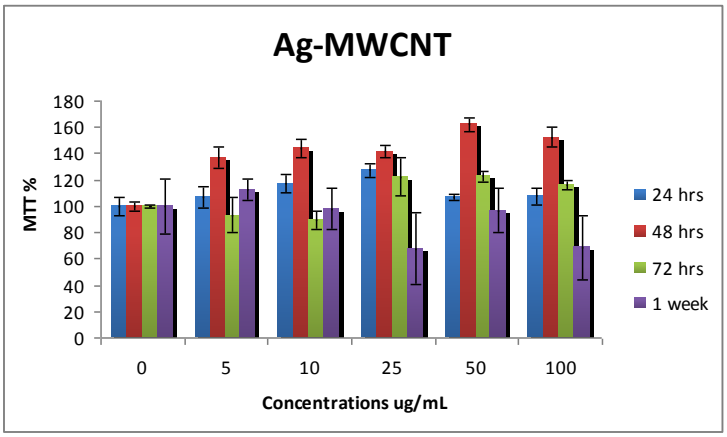

b.

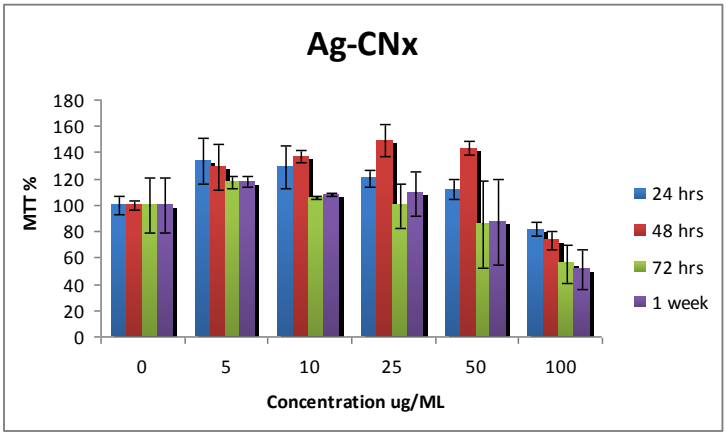

c.

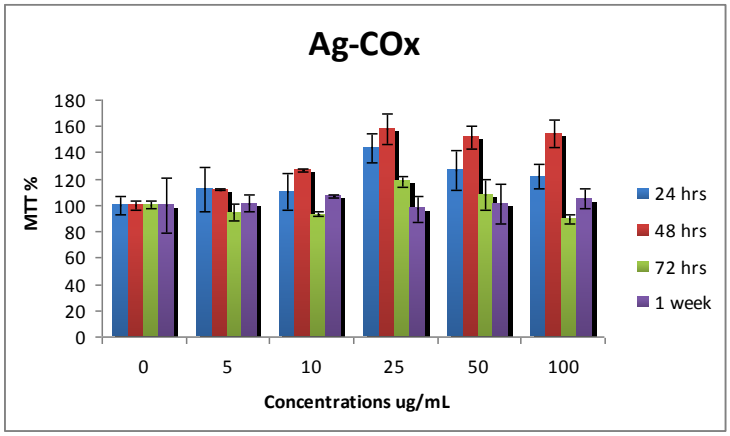

Figure 14. Cell viability in HaCaT cells exposed to different MWNT-Ag composites. Cell viability in HaCaT cells exposed to different MWNT composites. The cells were exposed to concentrations of 0, 5, 10, 25, 50 and 100µg/mL solutions of **(A)** Ag-MWNT, **(B)** Ag-MWNT-CNx and **(C)** Ag-MWNT-COx for 24 and washed . Recovery was then examined at 48h, 72h and 1 week.

Table 2. Summary Table showing particle size, cellular morphology, change in mitochondrial membrane potential (MMP), inflammatory response and recovery. There was a significant (*) decrease in MMP as well as a significant increase in TNF-α at 24h for Ag-MWNT and Ag-MWNT-COx.

Particle Type	Ave Diameter (nm)	Cell Morphology	MMP	PCR 6h fold increase		PCR 24h fold increase		MTS Recovery Cell Proliferation
				IL-6	TNF-α	IL-6	TNF-α	
Ag-MWNT	6.64	Minor Actin Disruption, Nuclear binding	* decrease	1.5	1.3	2.7	6.8	Increase
Ag-CNx-MWNT	8.82 & 12.70	No Disruption, Nuclear binding	* decrease	2.4	2.4	2	1.9	Increase
Ag-COx-MWNT	10.70 & 13.94	No Disruption, Nuclear binding	* decrease	2.6	2.5	.5	4	Increase

Evaluating the Biological Interactions of Nanomaterials Using Fluorescence Based Technology

Abstract

Currently there is no standardized method for making nanomaterials or evaluating their toxicity. Studies are showing great variability and lack of reproducibility in results, with the discrepancies as a result of the assays used to evaluate exposure toxicity. While the traditional biochemical methods for evaluating toxicity have been employed there is an issue of how the nanomaterials themselves interact with the dyes that has created some issues. The current methodologies need to be evaluated to determine the toxicity of the nanomaterials and ensure there is no interaction between the nanomaterials and the reagents used to complete the assays. This current study evaluated mechanisms of nanomaterial toxicity using mitochondrial function, loss of mitochondrial membrane potential, and formation of reactive oxygen species as indicators of toxicity, and compared the data obtained on the BD Pathway 435 to data from a plate reader, as well as presented nanoparticle uptake and localization. These studies demonstrated that the BD Pathway 435 provided more sensitive detection for the cellular based assays and was a useful tool for nanoparticle localization studies.

Introduction

Nanomaterials (NM) are playing an ever growing role in the consumer product industry. Currently NM, which are defined as having at least one dimension smaller than 100nm, are integrated into about 600 consumer products such as electronic components, cosmetics, cigarette filters, antimicrobial and stain-resistant fabrics and sprays, sunscreens, and cleaning products[37,38]. At this time the FDA has no regulations in place for any of these nano-items, but they are beginning to realize some regulations are necessary.

While nanomaterials have greatly improved our everyday life, they are also causing many health problems which can range from granuloma formation in the lung[39] to inflammation at the exposure site[40]. Reactive oxygen species formation has been shown to be the major mechanism of toxicity for nanoparticles[41]. Furthermore, it has been shown that there is an increase in toxicity as well as ROS production as silver particle size decreases in a study performed using rat alveolar macrophages[42]. Studies such as the one by Carlson show the need for future studies to evaluate the nanomaterials in comparison to their non-toxic bulk counterparts.

Over the past decade there has been a boom in the nanoparticle research field with around 100 articles written about gold and silver nanoparticles in 1990 to over 5,000 articles written in research journals in 2004 and the number is still growing[43]. Several of the studies and review papers have shown nanomaterials to be toxic, but still many questions regarding the health and environmental impact of these new "wonder" materials remain unanswered. Additionally, review papers have described technical

challenges associated with studying the unique properties of nanomaterials and how these properties correlate to the biological effects[44,45].

Currently there is no standardized method for making nanomaterials or evaluating their toxicity. Studies are showing great variability and lack of reproducibility in results, with the discrepancies as a result of the assays used to evaluate exposure toxicity. At this time, exposure protocols include evaluating mitochondrial membrane function, reactive oxygen species production, lactate dehydrogenase leakage assays and measuring the inflammatory response. While these are the traditional biochemical methods for evaluating toxicity the issue of how the nanomaterials themselves interact with the dyes has created some issues. The current methods need to be evaluated to determine the toxicity of the nanomaterials and ensure there is no interaction between the nanomaterials and the reagents used to complete the assays.

For example, some studies point to the MTT assay as being unreliable due to an interaction between nanomaterials such as carbon and formazan crystals[46]. The formazan crystals bind to the carbon nanotubes, so the crystals cannot be solubilized. Another study performed to examine the effects of aluminum nanoparticles in mammalian germ-line stem cells found it impossible to assess the naoparticle effects on mitochondrial function due to particle agglomeration and interference with plate reader measurements[47]. Other articles show the carbon nanotubes have negligible interaction with the formazan product and they do not influence the results of the study[48,49,50]. Due to the variability in NM and assays at this time, a method of examining the toxicity of nanomaterials, which can be used across all nanomaterial types and cell models needs to be identified.

Additionally, electron microscopy has been the only method used to verify uptake of nanomaterials and the sample preparation is labor intensive. Furthermore, the sample preparation for EM requires that the cells be fixed and the preparation can yield artifacts. Using the 3D imaging and fluorescent dyes, the uptake and localization of nanomaterials can be determined in a timely manner. Also, the BD confocal can be utilized for live or fixed cell imaging and the confocal filters out the background fluorescence, artifacts are not as readily observed. This current study evaluated mechanisms of nanomaterial toxicity using mitochondrial function, loss of mitochondrial membrane potential, and formation of reactive oxygen species as indicators of toxicity, and compared the data obtained on the BD Pathway 435 to data from a plate reader, as well as presented nanoparticle uptake and localization. These studies demonstrated that the BD Pathway 435 provided more sensitive detection for the cellular based assays and was a useful tool for nanoparticle localization studies.

Materials and Methods

BD Pathway 435

The BD Pathway was used for confocal imaging, as well as high content analysis for qualitative data collection. This instrument is a spinning disk confocal and in conjunction with the software BD Image Explorer the images can be analyzed to determine differences in fluorescent intensity to provide quantitative information.

Keratinocytes

The human keratinocyte cell line (HaCaT) was generously donated by the Army Research Lab[51]. The cells were cultured in a flask with RPMI-1640 media (ATCC) supplemented with 10% fetal bovine serum (FBS, ATCC) and 1% penicillin/streptomycin (Sigma) and incubated at 37˚C in a humidified incubator with 5% CO_2. For nanoparticle exposure procedures RPMI-1640 media was supplemented with 1% penicillin/streptomycin without serum.

The mouse keratinocyte cell line, HEL-30, was generously received from the Navy Research lab. The cells were cultured in flasks with a 1:1 mixture of Dulbecco's Modified Eagle's Medium/Nutrient F-12 Ham (DMEM/Ham's F-12, Sigma) supplemented with 10% fetal bovine serum (ATCC) and 1% penicillin/streptomycin (Sigma), and incubated at 37°C in a humified incubator with 5% CO_2. For nanoparticle exposure protocols, the DMEM/Ham's F-12 media was supplemented with 1% penicllin/streptomycin and no serum.

Male Germline Stem Cells

The C18-4 cell line[52] was grown in a 1:1 mixture of Dulbecco's Modified Eagle's Medium/Nutrient F-12 Ham supplemented with 10% fetal bovine serum (ATCC), 2 mM L-glutamine and 1% penicillin/streptomycin. Cells were incubated at 34°C and 5% CO_2 in a humidified incubator.

Osteoblasts

Human fetal osteoblast cells (hFOB 1.19, purchased from ATCC, CRL-11372) were cultured in 25-cm^2 tissue culture flasks at 37°C in a humidified atmosphere of 5%

CO_2 in air. A 1:1 mixture of Ham's F12 medium and Dulbecco's modified Eagle's medium was supplemented with 10% fetal bovine serum (FBS), and 0.3 mg/mL of G418 disulfate salt.

Nanoparticles

Carbon Foam

Microcellular carbon foam samples were purchased from Koppers Inc., in large blocks and then cut to fit in a 96 well plate. They were rinsed with Phosphate buffered saline (PBS) to remove any debris and sterilized under ultraviolet light prior to the seeding of cells. Double sided carbon tape was used to keep the foam adhered to the well and submerged in media during cell culture exposures.

Multi-walled Carbon Nanotubes

Multi-walled carbon nanotubes functionalized with silver and a nitrogen or carboxyl group were synthesized and received from Dr. Maurico Terrones of The Advanced Materials Department and Laboratory for Nanoscience and Nanotechnology Research, IPICYT, San Louis Potosi, Mexico.

Aluminum Nanoparticles

The aluminum oxide (Al_2O_3) 40 nm and aluminum (Al) 50 nm were synthesized and generously received in powder form from Dr. Karl Martin of NovaCentrix (formerly Nanotechnologies, Inc). The nanoparticles were weighed out and dispersed in water to create a stock solution at a concentration of 1 mg/ml.

Silver Nanoparticles

The Ag-25 nm nanoparticles were synthesized and generously received in powder form from Dr. Karl Martin of NovaCentrix (formerly Nanotechnologies, Inc). The nanoparticles were weighed out and dispersed in water to create a stock solution at a concentration of 1 mg/ml.

Ruthenium-labeled TiO_2 Nanoparticles

The 40 nm 100% anatase TiO_2 nanoparticles labeled with ruthenium (TiO_2-Ru) were generously donated to Wright-Patterson Air Force Base from Dr. Nina Joshi at UES, Inc.

Cellular Assays

Cell Viability Assays

The C18-4 cells were seeded at a density of 50,000 cells/well. Once the cells were 80% confluent in a 96-well plate, different concentrations of aluminum nanoparticles were added to the wells. The cultures were further incubated for 24 hours and then washed with PBS to remove any of the nanoparticles that had not been taken up by the cells. MTS was also performed on cells dosed with aluminum nanoparticles that had not been washed. Cell viability was evaluated using using the CellTiter 96®AQueous One Solution of Promega, which measures mitochondrial function and directly correlates to cell viability. The relative cell viability (%) related to control wells containing cell culture medium without nanoparticles or PBS as a vehicle was calculated by [A]test / [A] control x 100, where [A]test is the absorbance of the test sample and [A]control is the absorbance

of control sample. Each experiment was done in triplicate and the data are represented as the mean ± the standard deviation. A Student t test was performed and $p<0.05$ indicated significance. In addition, the Live Cell Dead Cell kit from Biovision was used to evaluate cell viability. The kit contains a green dye that is cell permeable and propidium iodide which is only permeable if the cells are dead. The ratio of red to green cells can be calculated to determine the changes in cell viability.

Reactive Oxygen Species

The HaCaT cells were seeded on a BD 96-well imaging plate at a density of 100,000 cells/well. Once the cells were 80% confluent they were dosed with 25μg/ml of different carbon nanotubes for 24h. Following exposure, the Image-iT® Live Reactive Oxygen Species (ROS) and the MitoSOX™ Red kits (Invitrogen) were used to evaluate the formation of ROS and superoxide, respectively according to the manufacturer's recommendations.

Mitochondrial Membrane Potential

The HaCaT cells were seeded on a BD 96-well imaging plate at a density of 100,000 cells/well. Once the cells were 80% confluent they were dosed with different carbon nanotubes for 24h. Following exposure, the MitE-ψ kit from Biomol International was used to evaluate changes in mitochondrial membrane potential according to the manufacturer's recommendations.

Image Acquisition and Data Analysis

For the endpoint assays, 16 fields in each well were imaged at 20X using the 4X4 montage option in the BD Pathway 435 software. For the ROS assays, the FITC and Hoescht filters were used and for the MitoSOX red assay, the Rhodamine and Hoescht filters were used. For the MitE-ψ assay and the Live Cell Dead Cell kit; the FITC, Rhodamine, and Hoescht filters were used. The images were then analyzed using the BD AttoVision™ v1.6 and the BD Image Data Explorer, which evaluated differences in fluorescent intensity between the samples. Additonally, for the MMP assay, plates were also read on the BioTek Synergy plate reader.

Cellular Morphology

Cellular Uptake and Localization

Osteoblast and Keratinocyte Actin Staining

For the cell morphology studies, 1.5 mL of hFOB suspension at a density of 1 x 10^6 cells/mL was plated in 24 well plates containing the carbon foam. The cells were incubated for 72 hours and then fixed with 4% paraformaldehyde at room temperature for 10 minutes. The cells were rinsed with PBS and permeabilized with 0.1% Triton X-100 for five minutes. The actin filaments were then stained with Alexa Fluor 555-phallodin from Invitrogen for 45 minutes. The samples were then rinsed with PBS and a few drops of Prolong Gold Reagent with DAPI nuclear counterstain were added. Foam

samples were then transferred to a BD 96-well imaging plate, inverted, and then imaged on the BD Pathway 435 confocal microscope.

The HaCaT cells were seeded on a LabTek Chamber at a density of 100,000 cells/well. Once the cells were 80% confluent they were dosed with different carbon nanotubes for 24h. Following exposure, the cells were fixed with 4% paraformaldehyde at room temperature for 10 minutes. The cells were rinsed with PBS and permeabilized with 0.1% Triton X-100 for five minutes. The actin filaments were then stained with Alexa Fluor 555-phallodin from Invitrogen for 45 minutes. The samples were then rinsed with PBS and a few drops of Prolong Gold Reagent with DAPI nuclear counterstain were added. The cells were then imaged using Cytoviva imaging ultra resolution microscopy[53].

Results and Discussion

Cellular Assays

Evaluation of Mitochondrial Membrane Potential

The mitochondrial membrane potential assay used the JC-1 dye to stain non-apoptotic cells red and apoptotic cells green based on how the dye interacts with the membrane potential. The confocal images illustrated that the negative control cells were non-apoptotic and the positive control cells treated with 100μM tert-butyl hydrogen peroxide (TBHP) showed non-apoptotic and apoptotic cells. Furthermore, the MWNT and CNx treated cells indicated that apoptosis was initiated with the CNx cells appearing to have more apoptosis initiated based on the images. Furthermore, the corresponding light images showed the presence of the nanomaterials in the cell cultures. (Figure 15 A-H). Additionally, following image acquisition, the ratio of red/green fluorescent intensity

within the images was determined using the BD Data Explorer program (Figure 15 I) which showed that there was a slight reduction in the positive control treatment, the MWNT, and the CNx treatments. The plate was also read on a plate reader to compare the data analysis techniques and the plate reader demonstrated a greater reduction in the red/green ratios for the different treatment groups. (Figure 15 J). Previous studies have found that carbon nanomaterials can react and absorb dyes and the mitochondrial membrane potential assay demonstrated that when a plate reader was used, higher fluorescent intensity measurements were recorded on the FITC setting, which in turn yielded lower red/green ratios indicating greater loss of MMP (Figure 15 J). These higher intensity measurements could be a result of the carbon nanomaterials absorbing the fluorescent dyes, since this did not correspond to what was observed microscopically, and when the fluorescent intensity was measured from the confocal images that were taken which eliminated the background measurements a more accurate measurement was obtained. The BD measurements demonstrated that the CNx initiated loss of MMP while the MWNTs only had minor disruptions (Figure 15 I).

Detection of Reactive Oxygen Species

Figure 16A-C evaluated the cellular morphology of human keratinocytes following exposure to Ag-carbon nanotubes with or without a nitrogen functional group attached. The actin and the nuclei in the keratinocytes were stained following a 24h exposure and imaged using ultra-resolution microscopy so that the carbon nanotubes were also visible. The control cells (Figure 16A) demonstrated a nice confluent monolayer with actin expression. The Ag-MWNTs (Figure 16B) illustrated that there were minor disruptions in the monolayer with a minimal decrease in actin expression. In

comparison, the keratinocytes treated with the Ag-MWNT-CNx resembled the control cells with a confluent monolayer and actin expression. Further studies evaluated the production of reactive oxygen species formation and superoxide formation in the presence of the nanotubes using the Image-iT® Live Reactive Oxygen Species kit (Figure 16D-G) and MitoSOX™ Red assays (Figure 2H-K). Figure 16D and 16E represent the negative and positive control respectively. The negative control showed little to no production of ROS while the positive control induced formation of ROS. The Ag-MWNTs and the Ag-MWNT-CNx generated ROS formation as well (Figure 16F and 16G respectively). Moreover, when the formation of superoxide was evaluated, the negative control showed little to no production (Figure 16H), the positive control demonstrated production of superoxide (Figure 16I) and the Ag-MWNTs induced formation of superoxide (Figure 16J) while the Ag-MWNT-CNx formed minimal amounts of superoxide. When evaluating the formation of reactive oxygen species, the levels of ROS observed by the Ag-MWNT-CNx was surprising since this treatment had not disrupted the morphology. The MitoSOX™ Red assay demonstrated that there was formation of superoxide in the presence of the Ag-MWNTs but not the Ag-MWNT-CNx, indicating that the nitrogen functional groups were capable of interacting with the ROS probe from the Image-iT® Live Reactive Oxygen Species kit (Figure 16). Therefore, the MitoSOX™ Red kit is a more sensitive method of detection when functional groups are present on nanomaterials.

Cellular Viability Assays

Carbon nanotubes are not the only nanomaterials that have interfered with biochemical assays. A previous study demonstrated that Al-NPs interfered with the MTS

assay and that accurate readings could not be obtained[47]. In this study, the C18-4 cells were treated with the aluminum nanoparticles and then morphology was assessed. In the control cells, there was expression of actin (Figure 18A) and at this nanoparticle dose the expression was drastically reduced in the Al_2O_3 treatment (Figure 18B) and non-existent in the Al treatment (Figures 18C). These morphological changes indicated that the nanoparticles were disrupting the cellular environment. When the C18-4 cells were treated with the Al-NPs and cellular viability was assessed after 24 h using the MTS assay, there did not appear to be a disruption in cellular proliferation (Figure 18D), which was contradictory to the morphology assay. However, when the excess nanomaterials were washed prior to performing the MTS assay, a reduction in cell viability was observed (Figure 18E), and this reduction occurred in a dose-dependent manner with the Al_2O_3 nanoparticles demonstrating the least toxicity. The validity of this washing technique was verified using the Live Cell/Dead cell assay from Biovision, which yielded results comparable to the MTS assay performed post-washing (Figure 18F). The cellular viability assays confirmed that the excess Al-NPs interfered with plate readings when the MTS assay was performed (Figure 18D-F). However, a simple washing step prior to running the MTS assay eliminated this problem (Figure 18E). Since nanomaterials can interfere with assays, verification of the data using another assay is critical, and since fluorescent assays tend to yield high levels of background on plate readers, the BD Pathway 435 provides a method for eliminating fluorescent background and verifying other assays using fluorescent based technology.

Cellular Localization and Uptake Studies

Osteoblast Colonization of Carbon Foam

Electron microscopy has been the only method available to demonstrate osteoblast growth on the carbon foam, and while this technique provides information on the osteoblast attachment and growth there are limitations. Using fluorescent microscopy, the osteoblasts can be labeled using immunofluorescence to detect markers of osteoblasts and osteoblast differentiation, however the propensity for the carbon foam to absorb fluorescent dyes makes this type of analysis problematic. The actin staining demonstrated that the confocal can filter out the background levels of fluorescence to distinguish the cells in the pores and on the edges of the foam making more in-depth cellular analysis possible. The carbon foam did absorb the Alexa-Fluor 555-phallodin dye (Figure 19A and 19B), however, the confocal was able to filter out some of the background from absorption so that the cells could be visualized and distinguished from the carbon foam (Figure 5). The carbon foam supported osteoblast growth in the pore (Figure 19A) and along the edges of the carbon foam (Figure 19B). Furthermore, it was demonstrated that the osteoblast cells were able to expand throughout the pore and form a network of cells with strong actin expression (Figure 19A and 19C).

Conclusion

This study has demonstrated that the properties of nanomaterials can make assessing the biological responses to these materials difficult. Some of the carbon nanomaterials absorbed the dyes or reagents used which results in inaccurate readings. In addition, functional groups added to the nanomaterials interacted with reagents to yield

false positive readings. The BD Pathway 435 provided a platform on which cellular based fluorescent assays were used and the problems associated with the false reading were corrected for since the evaluations were based on the images and what is being analyzed was controlled for. Furthermore, the confocal option on the BD Pathway 435 corrected the high levels of background associated with some of the fluorescence assays and nanomaterials. Additionally, background from metallic based nanoparticles was lessened through washing techniques which was confirmed using the BD Pathway 435. The BD Pathway 435 confocal microscopy also provided information on nanoparticle uptake using the 3D imaging and Z stack option, as well as, more information on nanoparticle localization in conjunction with cellular dyes. This microscopy technique is less labor intensive when compared to electron microscopy and the use of cellular stains and antibodies can provide more detailed information on cellular profiles and cellular interactions of the nanomaterials. Overall, the use of fluorescence based technology on a platform such as the BD Pathway 435 provides researchers with tools for assessing the biological interactions of nanomaterials that take into account some of the problems encountered with studying these materials with unique properties.

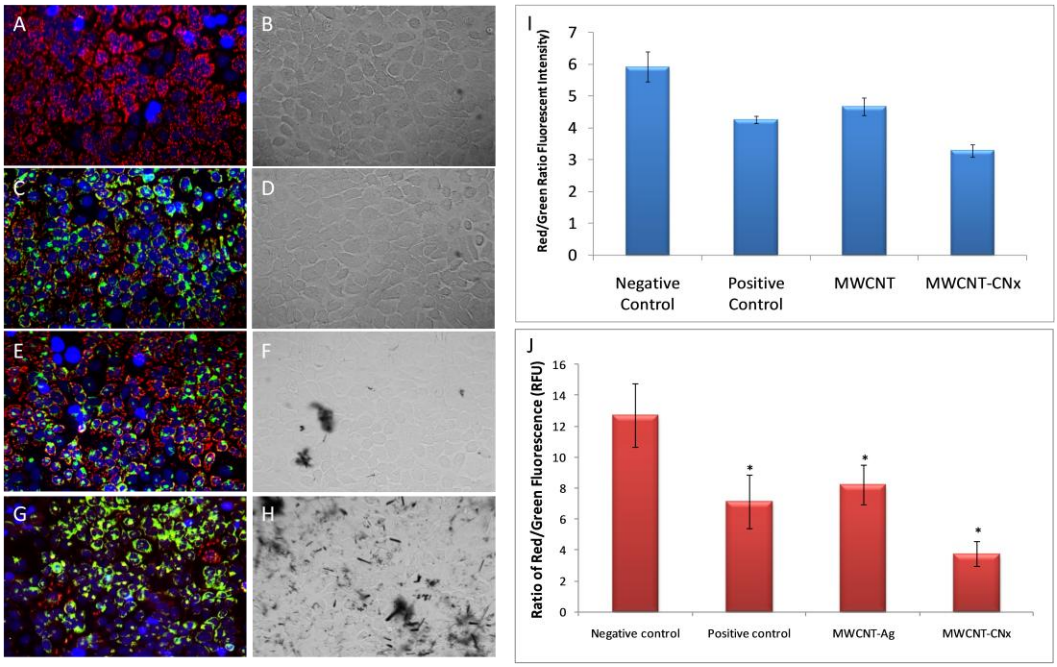

Figure 15. Measurement of Mitochondrial Membrane Potential in Carbon Nanotubes. A-H Confocal and light images of human keratinocytes following exposure to multi-walled carbon nanotubes. **I-J.** Measurement of fluorescent intensity. **A-B.** Negative Control, **C-D.** Positive Control, **E-F** Ag-Multi-walled carbon nanotubes, **G-H** Ag-Multi-walled nanotubes, **I**. Fluorescent intensity measurement using the BD Pathway 435. **J.** Fluorescent intensity measurement using a plate reader. The plate reader graph has higher intensity values due to background measurements. The BD Pathway 435 evaluated the intensity from the confocal images which eliminated the background fluorescences and gave a more accurate measurement.

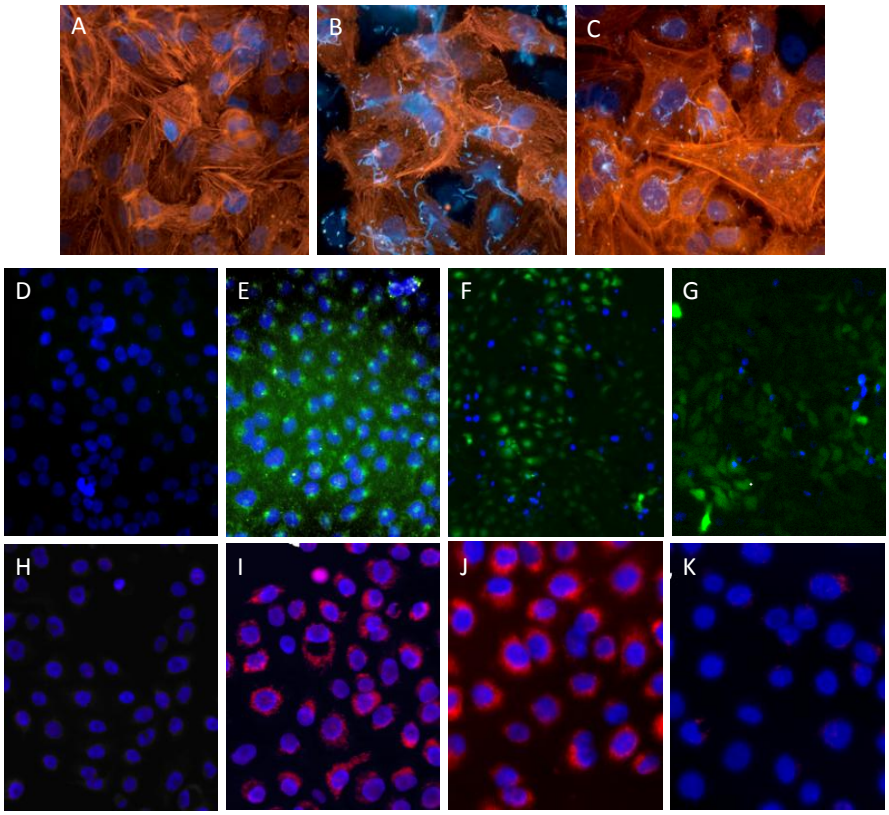

Figure 16. Measurement of Reactive Oxygen Species formation following carbon nanotube exposure. A-C Keratinocyte Morphology following 24 h exposure to various CNT. **D-G** ROS H-K MitoSox. **A-C**. Assessment of cell morphology following a 24 h exposure to carbon nanotubes. **A.** Untreated HaCaT cells. **B.** The cells treated with MWNTs have minimal disruption in the cell monolayer with little changes in actin staining in comparison to the control cells. **C.** The CNx carbon nanotubes did not demonstrate changes in the cell monolayer or actin staining indicating that they were biocompatible. **D-G.** Evaluation of reactive oxygen species in HaCaT cells following a 24 h exposure to carbon nanotubes. **D** Negative control, **E** Positive control, **F** MWNT, **G** CNx. The MWNTs and CNx nanotubes had similar levels of ROS production when the Image-iT Live ROS detection kit was used, which was not expected based on the morphology results, which showed that there was no disruption with the CNx. **H-K**. Evaluation of superoxide formation in HaCaT cells treated with carbon nanotubes. **H.** Negative control, **I**. Positive control, **J**. MWNT, **K**. CNx. When formation of superoxide was detected using the MitoSox red kit, the MWNTs produced superoxide while there was minimal expression of superoxide in the CNx treated cells which correlated to the morpholpogy data. This data suggested that the nitrogen components of the functional group added to the carbon nanotubes was reacting with the ROS Image-iT Live assay to produce nitrogen reactive species.

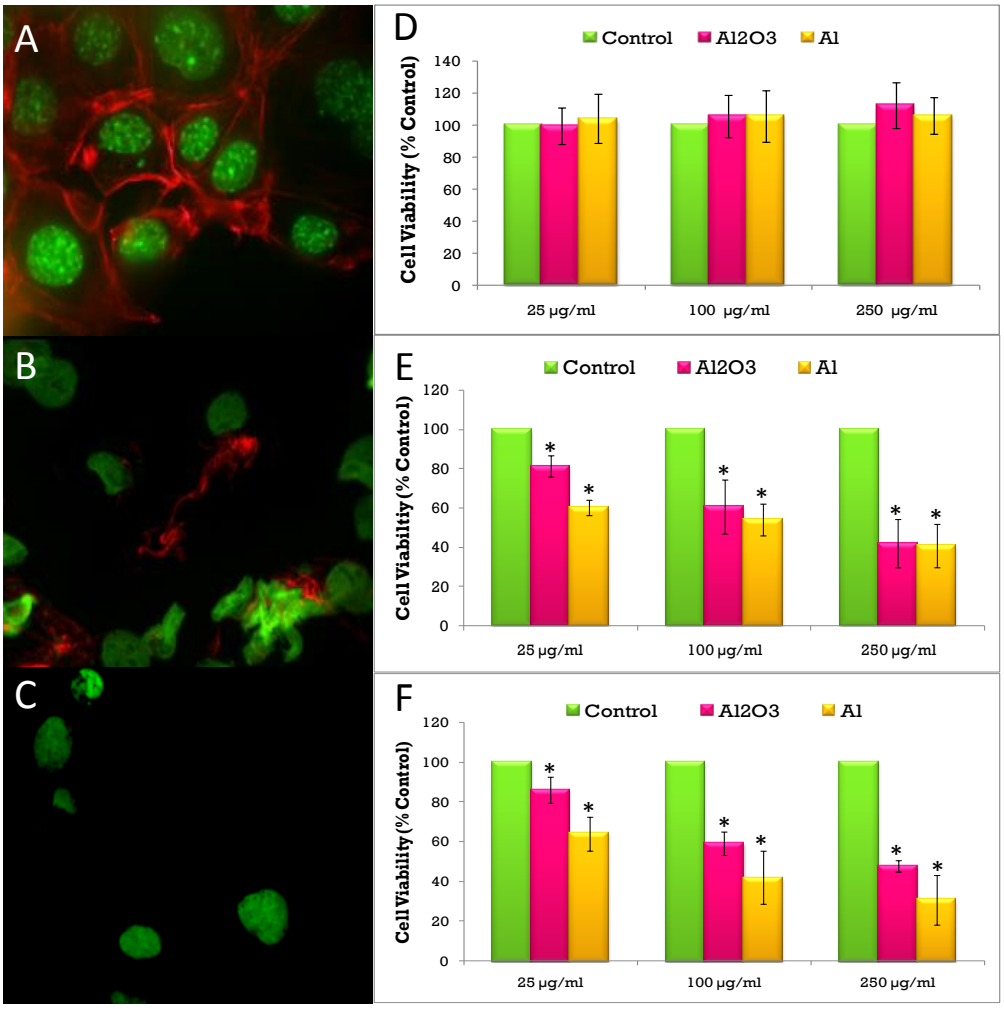

Figure 17. Cell viability measurements in germ-line stem cells treated with Al nanoparticles. A-C Confocal images of C18-4 cells with actin and nuclear staining. **A.** Control **B.** 100 µg/ml Al_2O_3 **C.** 100 µg/ml Al **D.** MTS measurement without washing following exposure. **E.** MTS measurement with washing following exposure. **F.** Live cell dead cell staining analyzed on the BD Pathway 435. The Al MTS that was run without washing was highly inaccurate and did not correspond to observed morphology changes **(A-C)**. When the excess Al nanoparticles were washed away prior to running the MTS assay, this greatly improved the measurement. Furthermore, the results from the washing technique were confirmed using the LCDC assay.

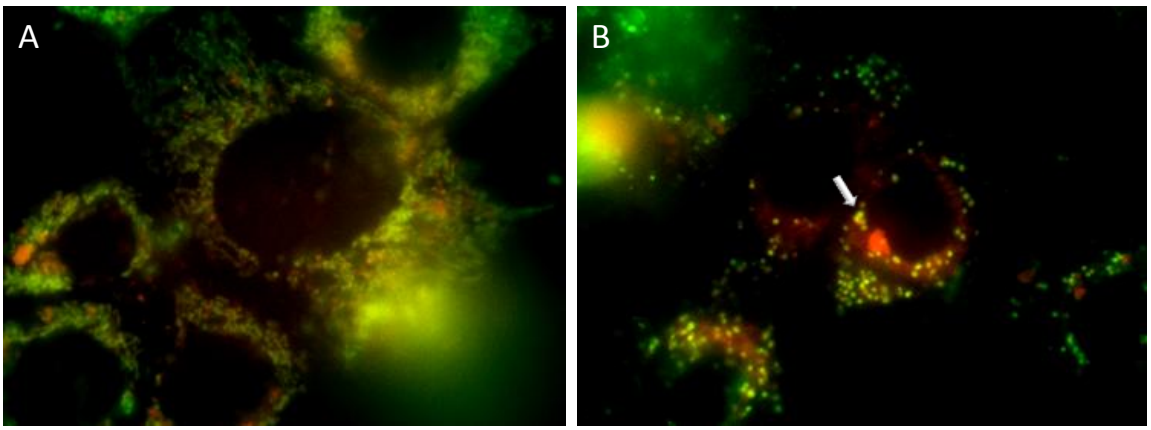

Figure 18. Nanoparticles localization in human keratinocytes.

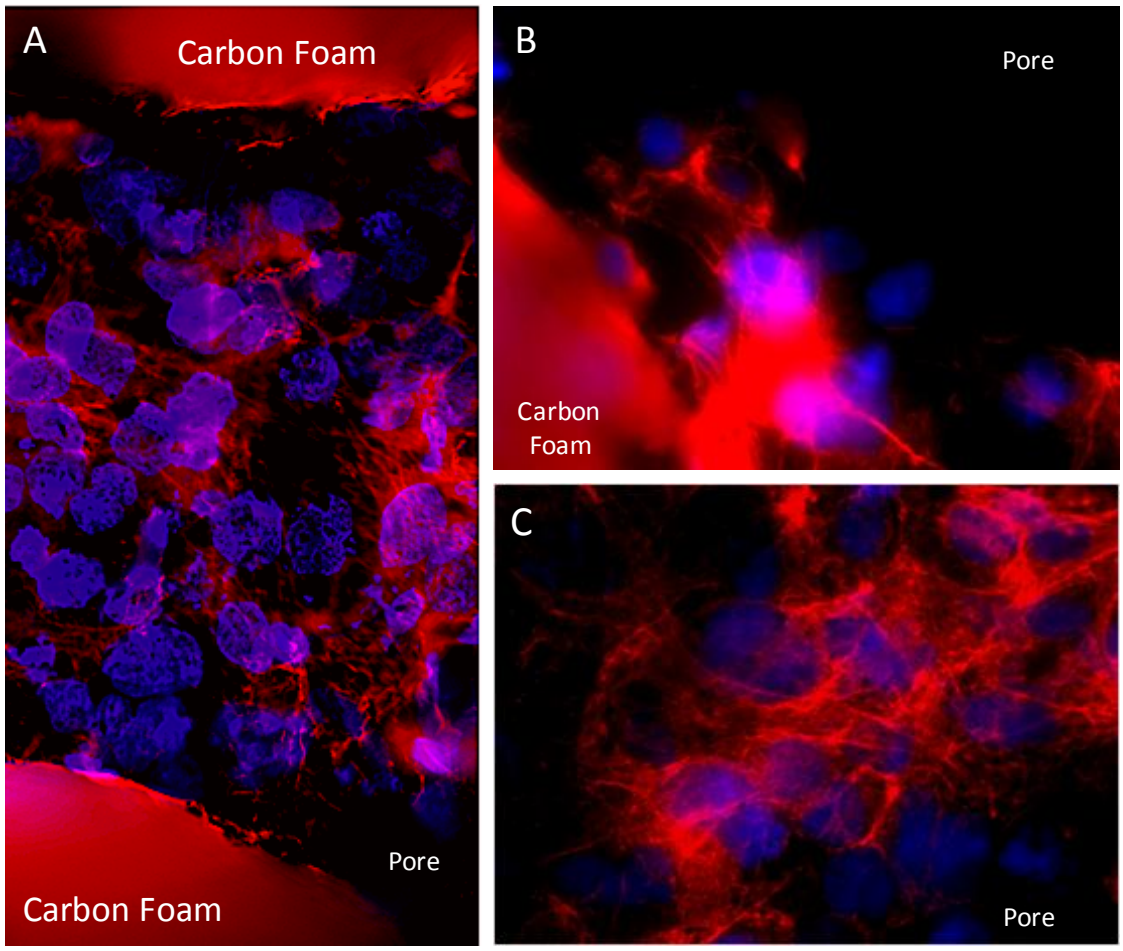

Figure 19. Osteoblast Growth on Carbon Foam. The osteoblasts were stained with Alexa 555-phallodin to visualize the actin in the cytoplasm and counterstained with the nuclear dye Hoescht 3334. The carbon foam absorbed the phallodin dye but using the confocal imaging to filter out some of the background, cells were seen colonizing the pores of the carbon foam. These osteoblasts expressed actin and can be seen attaching to the edges of the carbon foam pore and spreading out into the pore to form a cellular network.

In Vitro Biocompatibility of Nanoscale Zerovalent Iron Particles (NZVI) Synthesized using a Novel Green Chemistry Route

Abstract

A "green" protocol was used for the rapid generation of nanoscale zerovalent iron (NZVI) particles using tea polyphenols. The NZVI particles were subsequently examined for *in vitro* biocompatibility using the human keratinocyte cell (HaCaT) line as a skin exposure model. The cells were exposed to (ZVI) nanoparticles for time periods of 24 and 48 hours. Assessing the biocompatibility involved using the methyl tetrazolium, or MTS, (3-(4,5-dimethylthiazol-2-yl)-5-(3-carboxymethoxyphenyl)-2-(4-sulfophenyl)-2H-tetrazolium)) and Lactate dehydrogenase (LDH) assays to determine *in vitro* cytotoxicity following a short exposure. The evaluation of mitochondrial function (MTS) and membrane integrity (LDH) in human keratinocytes showed that these "green" synthesized NZVI particles were nontoxic in the human keratinocytes exposed. In fact, in most cases, these "green" nanoparticles induced a prolific response in the cellular functions even at the highest concentration (100µg/ml).

Introduction

Nanoscale zerovalent iron (NZVI) particles have been found to be effective in degrading various chlorinated organic contaminant hydrocarbons such as trichloroethylene[54], and trichloroethene (TCE)[55,57]. Recent environmental applications include removal of nitrite by ultrasound dispersed NZVI[58], dechlorination of dibenzo-P-dioxins[59], reduction of chlorinated ethane's[60], adsorption of humic acid and its effect on arsenic removal[61,62]. and hexavalent chromium removal[63]. However, field applications of NZVI have been limited to granular particles used in permeable reactive barriers (PRB)[57,58]. While PRBs are found to be effective for remediation of shallow aquifers, more cost-effective in situ technologies are lacking for rapid and complete destruction of chlorinated contaminants in deep aquifers and in source zones[58]. Recently, there is great interest in testing an in situ remediation strategy where reactive NZVI particles are directly delivered into the contaminant source zones compared to passive technologies such as PRB. The in situ preparation of the NZVI particles offers unique advantages, such as (i) the applicability to source zones in deep aquifers or to areas where lands are occupied and (ii) a much shorter overall remediation time (iii) transportation and chemical reactivity (iv) help relieving surface oxidation problems. However, for this technology to be feasible, the NZVI particles must be small enough to be mobile in the targeted zones, and the transport behaviors (or size) of the nanoparticles in various soils must be controllable. Yet, there has been no technique available for preparing NZVI particles of controlled size and transport properties, and a method is lacking to extend the

reactive lifetime of these relatively short-lived nanoparticles. There are several methods which have been employed to prepare NZVI particles including $NaBH_4$[64-67], ethylene glycol[68] and corbothermal synthesis[63]. While NZVI particles have been reported to be attainable by these methods, it was recognized that NZVI particles tend to rapidly agglomerate to form larger aggregates due to Van der Waals and magnetic forces, rendering them undeliverable to the targeted contaminant locations[64,65].

To prevent aggregation of metallic nanoparticles, particle stabilization has been commonly practiced by attaching a stabilizer such as a soluble polymer or surfactant onto the nanoparticles[66]. The stabilizer molecules are designed to provide strong inter-particle electrostatic and/or steric repulsions to outweigh the attractive Van der Waals and magnetic forces. To stabilize NZVI, two general strategies have been employed: (i) Use of stabilizers before the nanoparticles or aggregates are formed or (ii) to mechanically break down the formed nanoparticle agglomerates and add a stabilizer (post-agglomeration stabilization).

We have seen a renewed interest in using green chemistry principles in the preparation of nanomaterials and nanocomposites[67-80]. There is a tremendous increase in biological applications of these nanostructures, as well as a continuous interest in using biodegradable polymers or surfactants to cap these nanoparticles from the prevention of aggregation. Most of these polymers or surfactants have a tendency to be water soluble and it is of great interest to know how good dispersion or capping can be obtained using these biodegradable polymers or surfactants. The tea extract (poly phenols) was chosen

as a reducing agent and stabilizing agent because poly phenols are biodegradable (non toxic) and water soluble at room temperature, unlike other polymers. Second, poly phenols can form complexes with metal ions and thereafter can reduce the metals. Third, since tea extract contains molecules bearing alcoholic functional groups which can be exploited for reduction as well as stabilization of the nanoparticles.

In this paper we have synthesized green NZVI which can ideally be utilized for toxicological studies. Control experiments were carried out using the standard borohydride reduction method and results were compared with the new green approach. Favorable conditions to make Fe nanoparticles were established with uniform size and shape.

Experimental

Synthesis of "Green" Nanoscale Zero Valent Iron Particles (NZVI):

Tea extract preparation: About 2 grams of tea powder (Red label from Tata, India Ltd. 99%) was extracted in 100mLs hot water and then used to carry out the reaction with 0.1 N $Fe(NO_3)_3$. The different compositions were prepared at room temperature and are shown in Table-3. Control experiments were carried out using 0.1 N $NaBH_4$ solutions at room temperature and the compositions are listed in Table-3.

Nanomaterial Characterization:

Transmission electron microscopy (TEM) characterization was performed to obtain nanoparticle size and morphology on a Hitachi H-7600 tungsten-tip instrument at an accelerating voltage of 100kV. Nanoparticles were examined after suspension in water and subsequent deposition of 5 µL of solution onto formvar/carbon-coated TEM grids. The AMT software for the digital TEM camera was calibrated for size measurements of the nanoparticles at each magnification level. Information on mean size and standard deviation was calculated from measuring over 100 nanoparticles in random fields of view in addition to images that show general morphology of the nanoparticles.

Panalytical X-pert diffractometer with a copper Kα source was used to identify crystalline phases of the lead precipitates. The tube was operated at 45 kV and 40 mA for the analyses. Scans were performed over a 2-theta ranging from 5 to 70° with a step of 0.02° and a one-second count time at each step. Pattern analysis was performed by following ASTM procedures using the computer software Jade (Versions 8, Materials Data, Inc.), with reference to the 1995-2002 ICDD PDF-2 data files (International Center for Diffraction Data, Newtown Square, PA). UV spectra were recorded using Varian UV-visible spectrometer (Model Cary 50 Conc).

Keratinocyte (HaCaT) cell culture:

HaCaT cells were donated generously by Dr. James F. Dillman III, of the U.S. Army Medical Research Institute of Chemical Defense, . The HaCaT cells were cultured with RPMI-1640 media with 10% fetal bovine serum and 1% penicillin/streptomycin.

The HaCaT line was incubated at 37°C, 100% humidity, and 5% CO_2. During exposure, the HaCaT line was cultured with RPMI-1640 media with 1% penicillin/streptomycin and no fetal bovine serum (HEM).

Treatment protocol:

Cells were seeded to 60-80% confluency in 96 well plates within a growth period of 24-48 hours. Upon reaching 80% confluency, typically 48 hours, cells were treated with either 0µg/mL, 5µg/mL. 10µg/mL, 25 µg/mL, 50µg/mL or 100µg/mL concentrations of nanoparticles suspended in RMPI-1640 media with 1% Penicillin/Streptomicin. After a 24h or 48h exposure, the nanoparticle biocompatibility was assessed using cytotoxicity assays.

Cytotoxicity Assays:

The HaCaT cells were exposed to the NZVI at concentrations of 0µg/mL, 5µg/mL. 10µg/mL, 25µg/mL, 50µg/mL or 100µg/mL in RMPI-1640 media with 1% Penicillin/Streptomicin. After either 24h or 48h incubation with the nanoparticles, cell proliferation was measured using the CellTiter 96® Aqueous One Solution Cell Proliferation Assay (Promega), and membrane leakage were evaluated using the CytoTox 96® Non-Radioactive Cytotoxicity Assay (Promega). The mitochondrial function and membrane leakage were then assessed spectrophotometrically with a SpectraMAX Plus 190 microplate reader. The data are represented as an average of three independent trials ± the standard deviation.

Statistical Analysis:

The data are represented as an average of three independent trials ± the standard deviation. The cytotoxicity assays were run and any group with a p value less than 0.05 were considered significant.

Results and discussion

The reduction potential of caffeine is ~ 0.3 V vs. SCE which is sufficient to reduce metals viz. Fe (reduction potential -0.44 V vs. SCE). The formation of Fe nanoparticles with caffeine/polyphenols took place via the following steps: (1) complexation with Fe salts, (2) simultaneous reduction of Fe (3) capping with oxidized polyphenols/caffeine. The reduction of Fe was confirmed using UV spectra and is shown in Figure 20. The blank extract has an absorption beginning at 500 nm which is similar to the control $Fe(NO_3)_3$ solutions. The reaction between $Fe(NO_3)_3$ and tea extract was instantaneous and the color of the reaction mixture changed from yellow to dark brown as shown in the inset of Figure-20. After the reaction the UV spectra had broad absorption at a higher wavelength and there was no sharp absorption at lower wavelengths as shown in the controls.

UV spectra of T1, T2, T3, T4, T5 and T8 are shown in Figure 21. All the spectra looked similar in the visible region, but displayed slight differences in the UV region. T1 and T8 did not show strong absorption in the UV range when compared with T2 and T5.

The spectra of T3 and T5 had sharp absorption in the UV range when compared with all the others plotted.

X-ray diffraction (XRD) experiments were conducted to confirm the phase formation. Figure 22 shows the XRD pattern of T1, T2, T3, T4 and T8 samples respectively. Except sample T2, all the patterns showed a 100% intensity peak around 2θ 50^0 and could be indexed to hexagonal Fe (JCPDS No. 00-024-0072). The XRD pattern of T2 showed 100% intensity peak at 2θ, 33.115 which can be indexed to rhombohedraphase of alpha Fe_2O_3 with plane (104).

Figure 23 shows TEM images of T1, T2, T3 and T4 samples respectively. Sample T1 yielded spherical particles ranging from 40 to 50 nm whereas T2 and T3 yielded ultra small nanoparticles which are difficult to visualize at this magnification. However, sample T4 showed different structures such as platelets and nanorods. We believe concentration of tea extract plays a key role in dictating the final structures and size of the iron nanoparticles. Sample T4 contained minimal amounts of caffeine/polyphenols hence the larger the particle size. Caffeine/polyphenols are important for reducing and capping behavior[72]. At higher caffeine/polyphenols concentrations in the reaction mixture we observed a decrease in particle size.

Figure 24 shows the shape of the particles found in samples T5-T8, which were found to be spherical and larger in size when compared with T1 to T4. The control samples C1 and C2 formed irregular shapes with size varying from 50 nm (control C1) to nearly 500 nm (control C2) as shown in figure 25.

The MTS assay of all the tested samples at 24 and 48 h showed no decreases in cell proliferation similar to control samples (see Figure 26 and Figure 27). LDH leakage results after 24h didn't show any discernible difference from control samples except in samples T1, T2, T3, and T4, but after 48h results were significantly higher when compared with control samples indicating an increase in membrane leakage in HaCaT cells treated with NZVI (see Figure 28-33). T1, T2, T3 and T4 showed increases in LDH leakage when the particle concentrations reached 50µg/mL and above.

Conclusion

A "green" one-step approach has been developed for the synthesis of nanoscale zerovalent iron particles at room temperature. The method does not use typical noxious chemical reducing agent or a surfactant and can be scaled up to bulk level. The "green" synthesized NZVI samples were assessed with MTS and LDH toxicological assays and some of them were found to be nontoxic when compared with control samples prepared using the conventional borohydride reduction protocols. This simple method offers spherical zerovalent iron nanoparticles with unique size and shape when compared with control samples. We anticipate the development of various technological and environmental remediation applications for these particles including dechlorination of

dibenzo-P-dioxins, reduction of chlorinated ethanes, arsenic and hexavalent chromium removal to name a few.

Table 3. Compositions of the reaction mixtures for various samples.

Sample Code No	Description
T1	10mL tea extract + 1mL 0.1N $Fe(NO_3)_3$ solution
T2	5mL tea extract + 5mL 0.1N $Fe(NO_3)_3$ solution
T3	1mL tea extract + 5mL 0.1N $Fe(NO_3)_3$ solution
T4	1mL tea extract + 10mL 0.1N $Fe(NO_3)_3$ solution
T5	5mL tea extract + 4mL 0.1N $Fe(NO_3)_3$ solution
T6	5mL epicatechin (.01N) extract + 1mL 0.1N $Fe(NO_3)_3$
T7	4mL epicatechin (.01N) extract + 4mL 0.1N $Fe(NO_3)_3$
T8	5mL tea extract + 2mL 0.1N $Fe(NO_3)_3$ solution
C1	Control 2mL $Fe(NO_3)_3$ + 10mL $NaBH_4$
C2	Control 1mL $Fe(NO_3)_3$ + 10mL $NaBH_4$
C3	Control 1mL Fe(NO3)3 + 5mL NaBH4

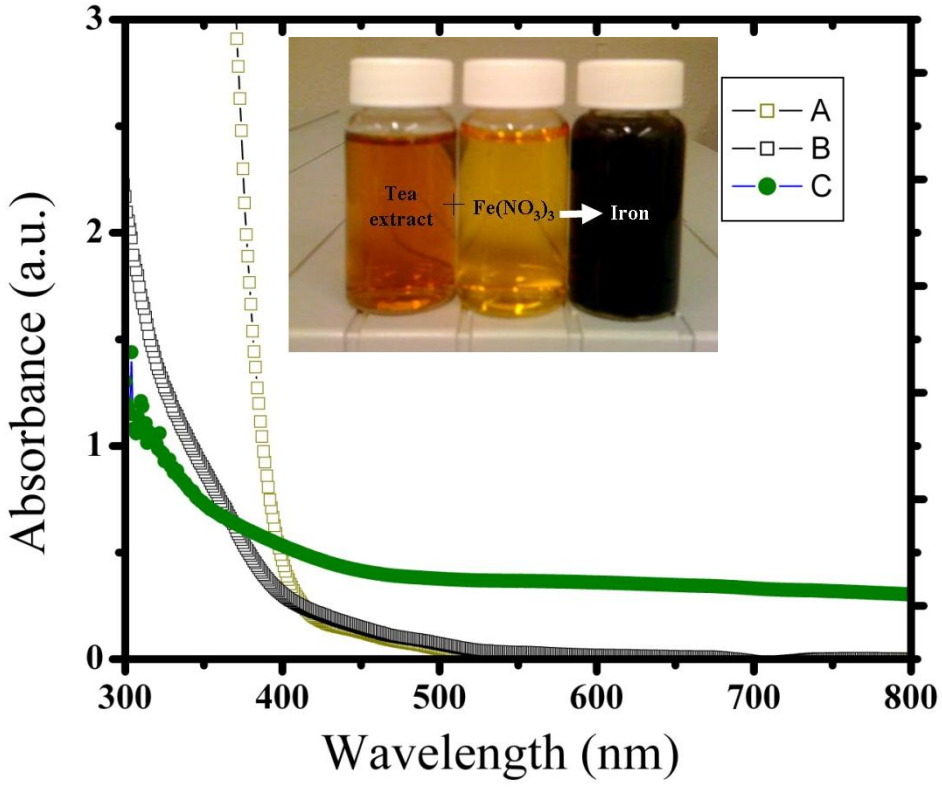

Figure 20. UV spectra of **(a)** Fe, **(b)** tea extract and **(c)** reaction product of $Fe(NO_3)_3$ and tea extract. The wavelength around 400nm is characteristic of Fe, and is not shown in the tea extract. Inset shows the photographic image of the reaction.

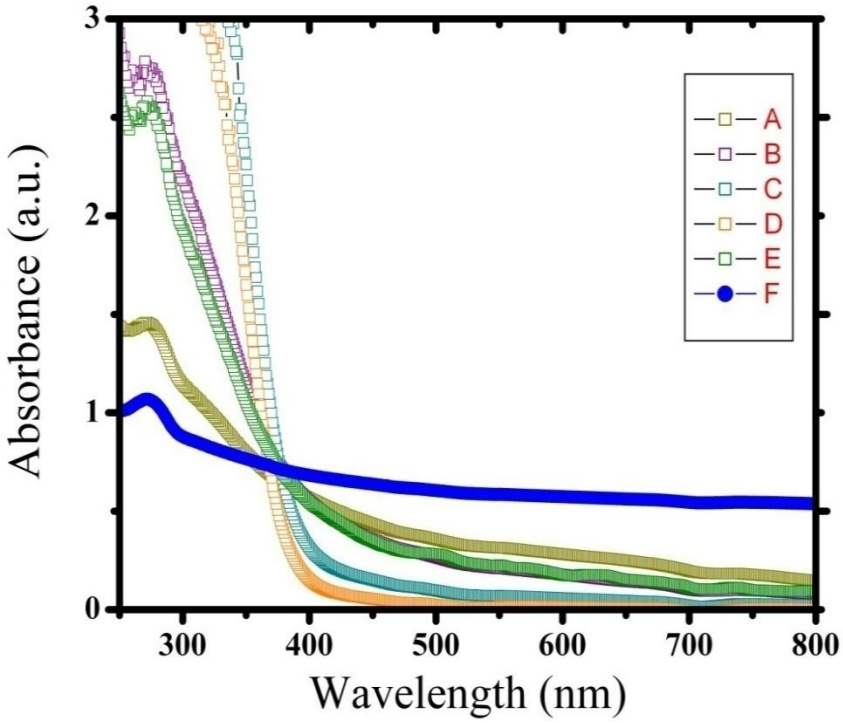

Figure 21. UV spectra of **(A)** T1, **(B)** T2, **(C)** T3, **(D)** T4, **(E)** T5 and **(F)** T8 samples showing the expected wavelength of iron around 400nm.

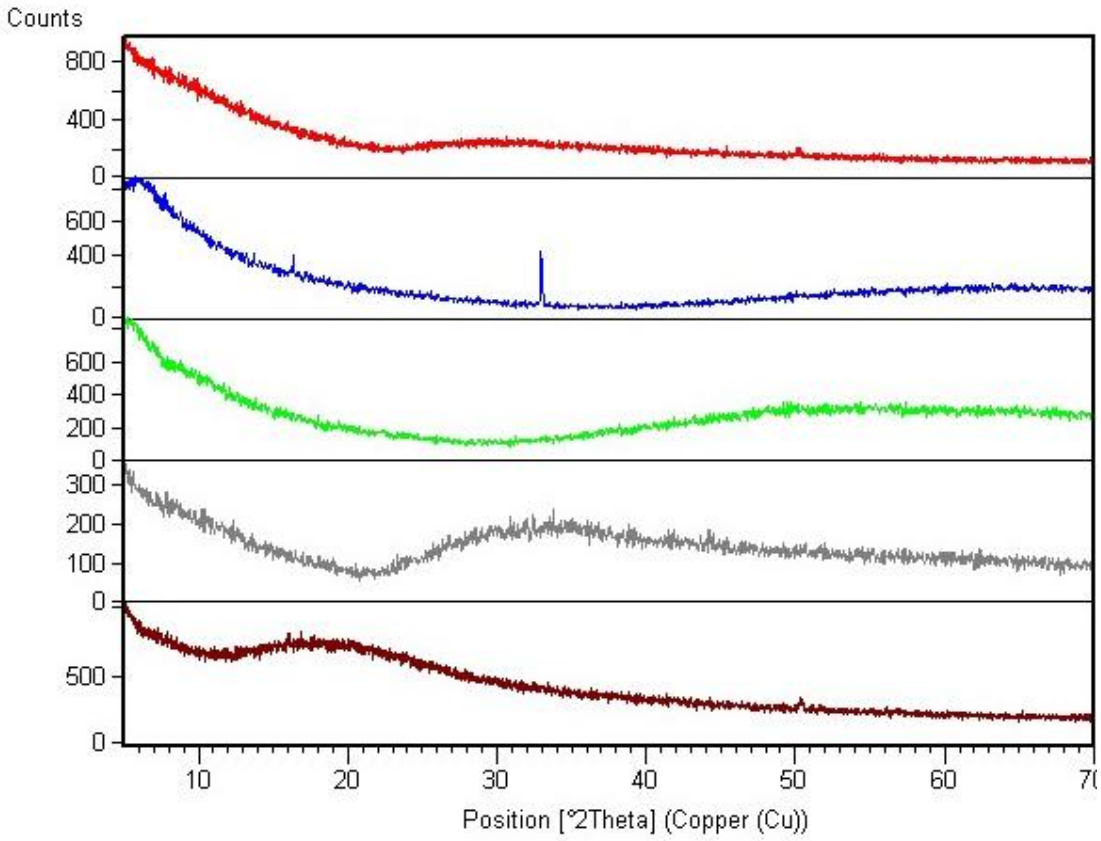

Figure 22. XRD pattern of **(a)** T1 top **(b)** T2 **(c)** T3 **(d)** T4 and **(e)** T8 samples

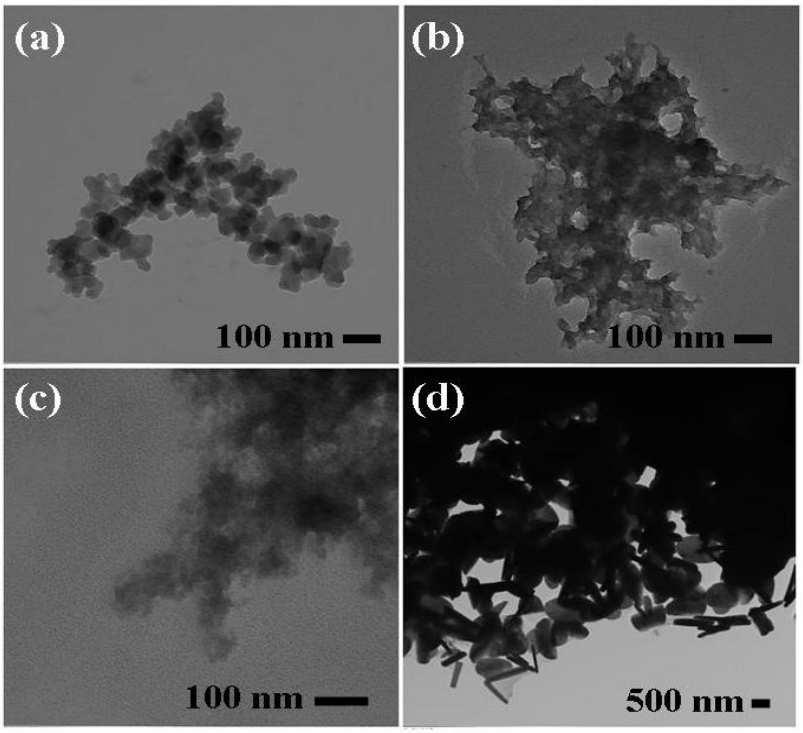

Figure 23. TEM images of **(a)** T1, **(b)** T2, **(c)** T3 and **(d)** T4 samples.

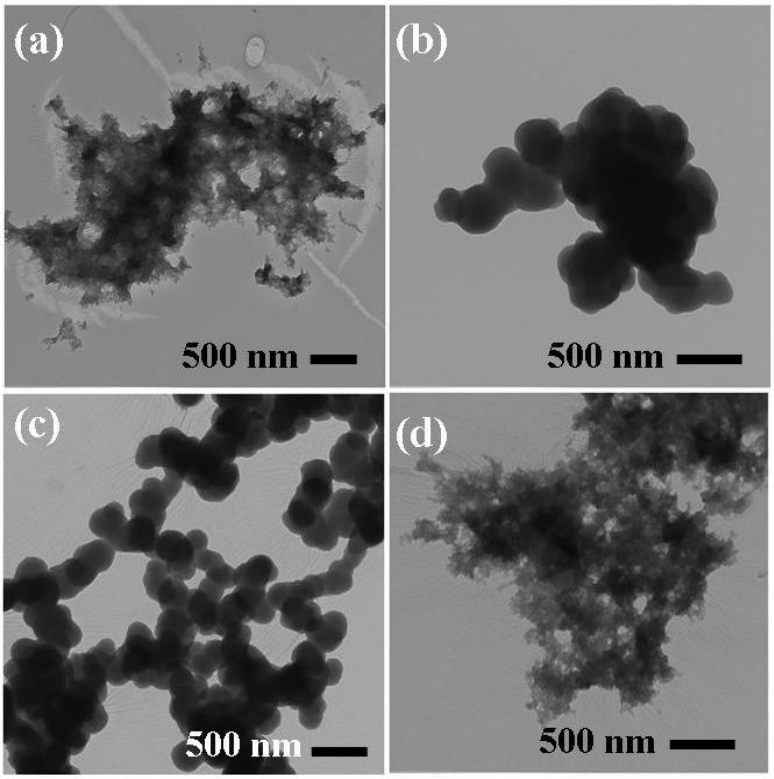

Figure 24. TEM images of **(a)** T5, **(b)** T6, **(c)** T7 and **(d)** T8 samples.

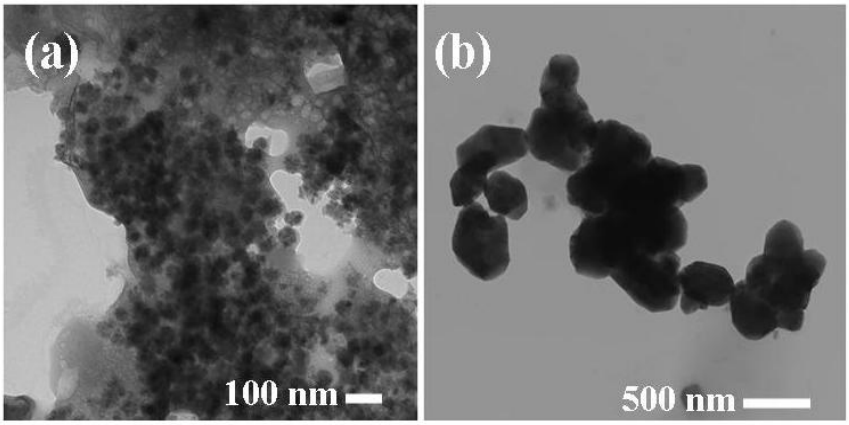

Figure 25. TEM images of **(a)** C1 and **(b)** C2 control samples.

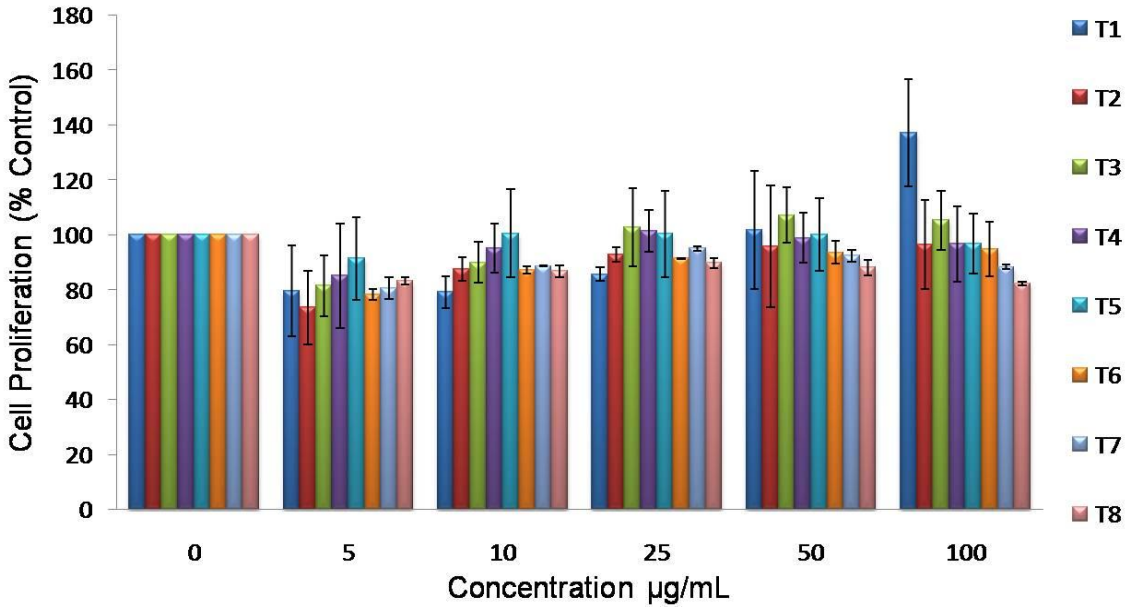

Figure 26. MTS Cell Proliferation Assay after 24h Exposure to NZVI. The results show no significant reductions in cell proliferation after 24h of exposure to the nanomaterials.

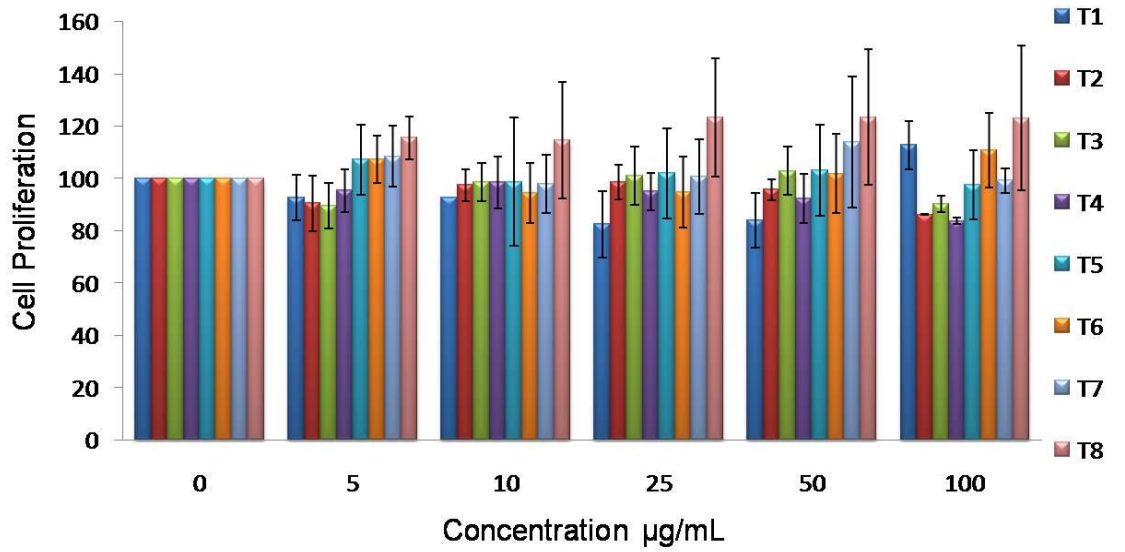

Figure 27. Cell Proliferation MTS Assay after 48h exposure to NZVI. The results show no significant reductions in cell proliferation after 48h of exposure to the nanomaterials.

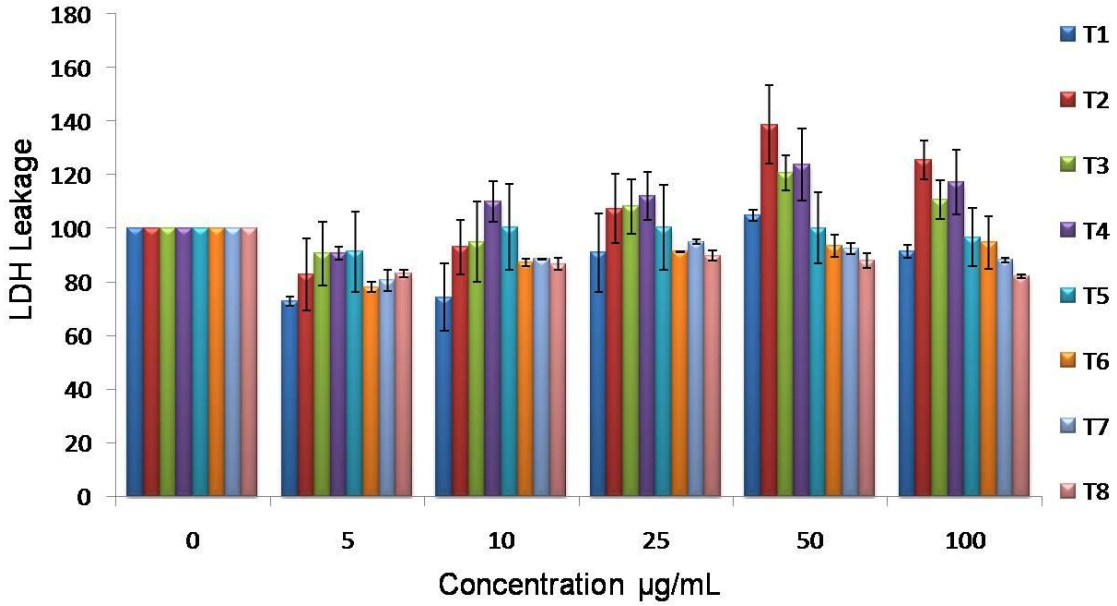

Figure 28. Lactate Dehydrogenase (LDH) Leakage after 24h exposure to NZVI

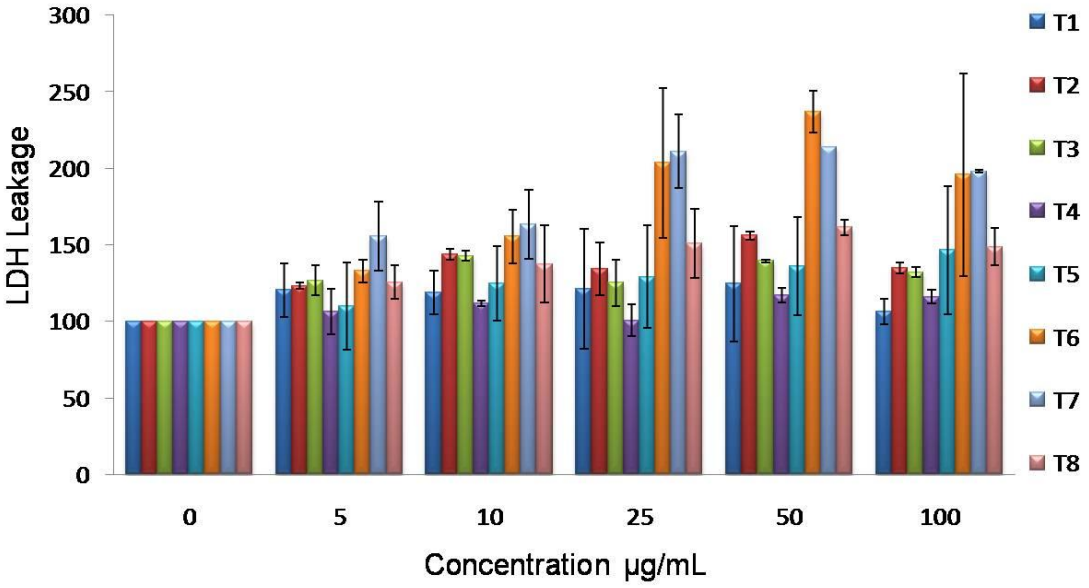

Figure 29. Lactate Dehydrogenase (LDH) Leakage after 48h exposure to NZVI

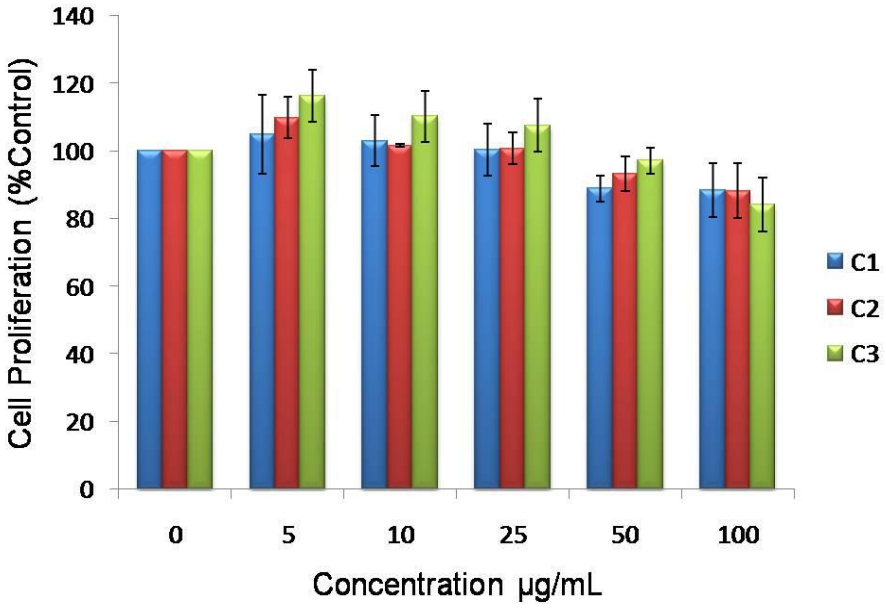

Figure 30. Cell Proliferation MTS Assay after 24h exposure to Control Particles

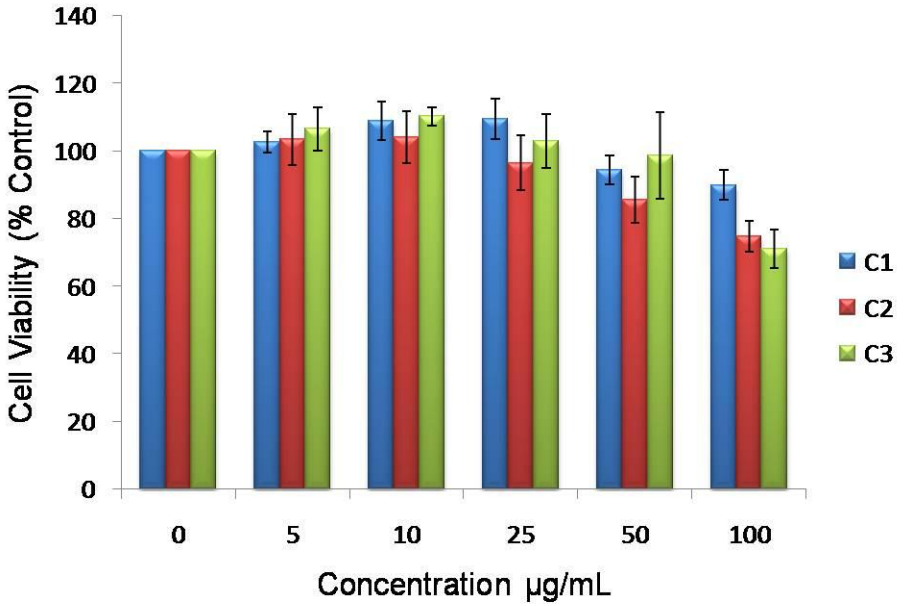

Figure 31. Cell Proliferation MTS Assay after 48h exposure to Control Particles

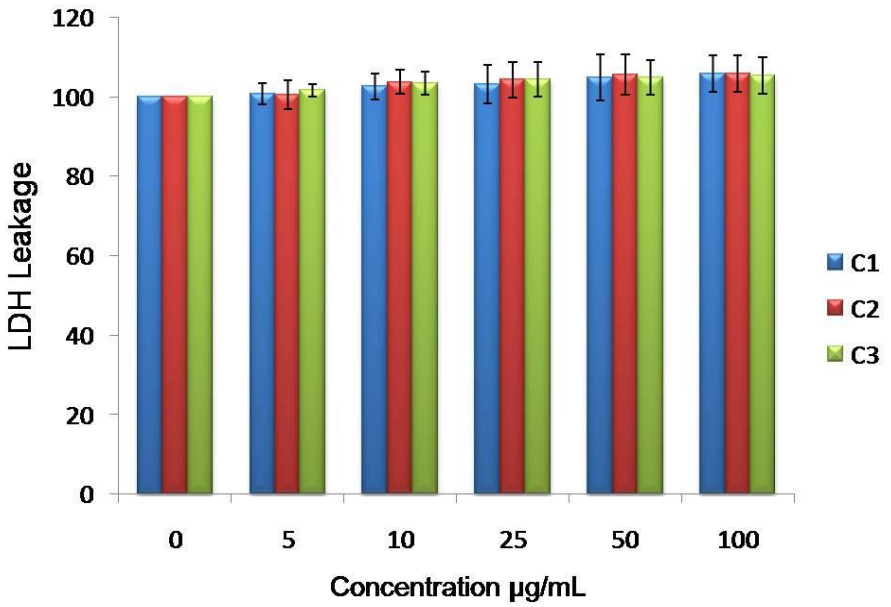

Figure 32. Lactate Dehydrogenase (LDH) Leakage after 24h exposure to Control Particles

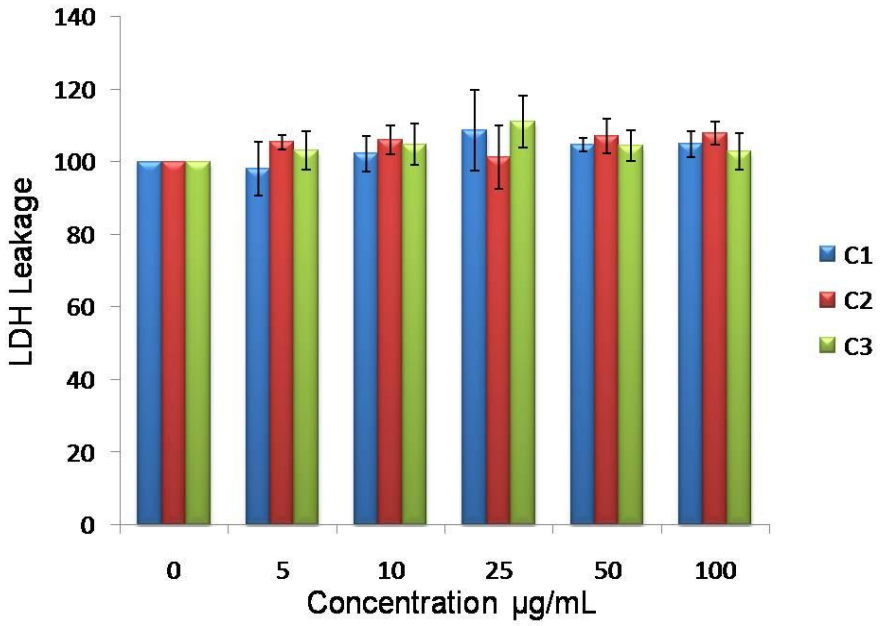

Figure 33. Lactate Dehydrogenase (LDH) Leakage after 48h exposure to Control Particles

References

1. Oberdorster, G., Maynard, A., Donaldson, K., Castranova, V., Fitzpatrick, J., Ausman, K., Carter, J., Karn, B., Kreyling, W., and Lai, D. *Part Fibre Toxicol.*, **2005**, 8.
2. Thomas, K., and Sayre, P. Toxicol. Sci., **2005**, 316-321
3. Bernadette A. Hernandez-Sanchez, Timothy J. Boyle*, Timothy N. Lambert, Sherrika D. Daniel-Taylor, *IEEE Transactions on Nanobioscience*, **2006**.
4. Ming-qi Gu, Xu-bo Yuan, Chun-sheng Kang, Yun-hui Zhao, Neng-jiang Tian,Pei-yu Pu, Jing Shengy,. *Carbohydrate polymers*, **2007**, 417–426
5. Kumar S, Harrison N, Richards-Kortum R and Sokolov K, *Nano Lett*, **2007**, 1338–43
6. LesniakW, Bielinska A U, Sun K, Janczak K W, Shi X, Baker J R Jr and Balogh L P, *Nano Lett*,**2005**, 2123–30
7. Chen, C.-D.; Cheng, S.-F.; Chau, L.-K.; Wang, C. R. C., *Biosens. Bioelectron*. **2007**, 926-932.
8. www.sharperimage.com
9. V.Alt, T.Bechert, P.Steinrucke, M.Wagener, P.Seidel, E.Dingeldein, E.Domann and R.Schnettler: *Biomaterials*, **2004**, 25(18), 4383.
10. Georgia Institute of Technology, Copyright 2006 NNIN-1025, http://www.nnin.org/doc/NNIN-1025.pdf
11. Hogan H, *Nanophotonics*,**2008**.
12. Carlson, Cataleya; Hussain, Saber; Schrand, Amanda; Braydich-Stolle, Laura; Hess, Krista; Rochelle, Jones; Schlager, John. *The Journal of Physical Chemistry*
13. Hussain, S., Meneghini, E., Moosmayer, M., Lacotte, D., and Anner, B.M., *Biochim. Biophys. Acta* 1994, *2*, 402-408.
14. J.R.Morones, J.L.Elechiguerra, A.Camacho, K.Holt, J.B.Kouri, J.T.Ramirez and M.J.Yacaman: *Nanotechnology*, **2005**, 16(10), 2346.
15. Amanda M. Schrand, Laura K Braydich-Stolle, John J Schlager, Liming Dai, Saber M Hussain. *Nanotechnology*, **2008**, 235104 (13pp).
16. Laura Braydich-Stolle, Saber Hussain, John J. Schlager, and Marie-Claude Hofmann, *Toxicological Sciences*, **2005**, 412-419.
17. Erik T. Thostenson, Zhifeng Ren, Tsu-Wei Chou, *Composites Science and Technology*, **2001**, 1899-1912
18. Fan S, Chapline MG, Franklin NR, Tombler TW, Cassell AM,Dai H., *Science*, **1999**, 512–4.
19. Wong SS, Joselevich E, Woolley AT, Cheung CL, Lieber CM., *Nature*,**1998,** 52–5.
20. Yao Z, Postma HWC, Balents L, Dekker C., *Nature* **1999**, 273–6.

21. A.A. Shedova, ER Kisin, D. Porter, P. Schulte, V.E. Kagan, B. Fadeel, V. Castranova. *Pharmacology and Therapeutics*, **2009**, 192-204
22. Challa S.S.R. Kumar *Biofunctionalization of Nanomaterials*, **2005**, 49-51
23. Anna Shvedova; Vincent Castranova ; Elena Kisin; Diane Schwegler-Berry; Ashley Murray; Vadim Gandelsman; Andrew Maynard; Paul Baron. *Journal of Toxicology and Environmental Health, Part A.*, 2003,1909-1926.
24. L.E. Murr, K.M. Garza, K.F. Soto, A. Carrasco, T.G. Powell, D.A. Ramirez, P.A. Guerrero, D.A. Lopez and J. Venzor III, *Int. J. Environ. Res. Public Health*, **2005**, 31–42.
25. Poland CA, Duffin R, Kinloch I, Maynard A, Wallace WA, Seaton A, Stone V, Brown S, Machee W, Donaldson K. *Nature Nanotechnology*, **2008**, 423-428
26. Hu H, Ni Y, Montana V, Haddon RC, Parpura V. *Nano Lett* **2004**, 507–511.
27. Elias KL, Price RL, Webster TJ, *Biomaterials*, **2002**, 3279-2787
28. Christin Grabinski, Saber Hussain, Khalid Lafdi, Laura Braydich-Stolle, John Schlager. *Carbon*, **2007**, 2828-2835
29. Andre New, Tian Xia, Lutz Madler, Ning Li., *Science* **2006**, 622-627
30. http://z.about.com/d/dermatology/l/0/e/4/Epidermis_Full_lucid.jpg
31. Masakazu Yoshizumi, Tadashi Nakamura, Masahiko Kato, Taisei Ishioka, Kunihisa Kozawa, Kaori Wakamatsu and Hirokazu Kimura, *Cell Biology International*, **2008**, 1405-1411.
32. Alexander Johnson, Bruce Alberts, Julian Lewis *Molecular Biology of the* Cell, **2002**.
33. M. Mayne, N. Grobert, M. Terrones, R. Kamalakaran, M. Rühle, H.W. Kroto, D. R. M. Walton, Chem. *Phys. Lett.* **2001**,101–107.
34. Botello-Méndez, A.R., Campos-Delgado, J., Morelos-Gómez, A., Romo-Herrera, J.M. Rodríguez, A.G., Navarro, H., Vidal, M.A., Terrones, H., Terrones, M. *Chemical Physics Letters*, **2008**,55-61.
35. Paul W. Barone, Seunghyunbaiki, Daniel A Heller, Michael S. Strano. *Nature Materials*, **2005**, 86-92.
36. Jinping Cheng, Chung Man Chan, L. Monica Veca, Wing Lin Poon, Po Kwok Chan, Liangwei Qu, Ya-Ping Sun, Shuk Han Cheng. *Toxicol and Appl Pharmacol*., **2009**, 216-225.
37. Woodrow Wilson International Center for Scholars, http://www.nanotechproject.org.
38. Hansen, S. F., Michelson, E. S., Kamper, A., Borling, P., Stuer-Lauridsen, F., and Baun, A., *Ecotoxicology*, **2008**, 438–447.
39. Warheit, D. B., Laurence, B. R., Reed, K. L., Roach, D. H., Reynolds, G. A., and Webb, T. R. *Toxicol. Sci*, **2004**, 117-125.
40. Hoet P, Briusle-Hohlfeld I, Salata O. *J Nanobiotechnol*, **2004**, 2(1): 12

41. Nel A, Xia T, Madler L, Li N.Science, **2006**, 622-27.
42. Carlson C, Hussain SM, Schrand AM, Braydich-Stolle LK, Hess KL, Jones RL, Schlager JJ. *J Phys Chem*, **2008** 209-17.
43. Eustis S and el-Sayed MA. *Chem Soc Rev*, **2006**, 209-217
44. Stern ST and McNeil SE., *Toxicol Sci.* **2008,** 4-21.
45. Hussain SM, Braydich-Stolle LK, Schrand AM, Murdock RC, Yu KO, Mattie DM, Schlager JJ, and Terrones M. *Adv Mater*, **2009**, 1-11.
46. Worle-Knirsch JM, Pulskamp K, Krug HF *Nano Letters*, **2006**,1261-8
47. Braydich-Stolle, L., Hussain, S., Schlager, J. J., and Hofmann, M. C., *Toxicol. Sci.* **2005**, 412-419.
48. Grabinski, C.M., Hussain, S.M., Lafdi, K., Braydich-Stolle, L., Schlager, J.J. *Carbon*, **2007**,2828-2835.
49. Schrand A.M, Huang H., Carlson C., Schlager J.J., Omacr Sawa E., Hussain S.M., and Dai L., *J. Phys. Chem B*, **2007**, 2-7.
50. Wick P, Manser P, Limbach LK, Dettlaff-Weglikowska U, Krumeich F, Roth S, Stark WJ, Bruinink A., *Toxicol Lett* **2007**, 121-31.
51. Boukamp P, Petrussevska RT, Breitkreutz D, Hornung J, Markham A, Fusenig NE, *J Cell Biol*, **1988**, 761–771
52. Marie-Claude Hofmann, Laura Braydich-Stolle, Luis Dettin, Eric Johnson, Martyn Dym. *Stem Cells* **2005**, 200-210.
53. Jeanne E. Skebo, Christin M. Grabinski, Amanda M. Schrand, John J. Schlager and Saber M. Hussain. *International Journal of Toxicology*, **2007**, 135-141
54. K. –C. Huang, S. H. Ehrman, *Langmuir* **2007**, *23(3)*, 1419.
55. Q. Huang, X. Shi, R. A. Pinto, E. J. Petersen, W. J. Weber Jr., *Environ. Sci. Technol.* **2008**, *42(23)*, 8884.
56. L. Guo, Q.-J. Huang, X.-Y. Li, S. Yang, *Langmuir* **2006**, *22(18)*, 7867
57. S. R. Kanel, R. R. Goswami, T. P. Clement, M. O. Barnett, D. Zhao, *Environ. Sci. Technol.* **2008**, *42(3)*, 896.
58. F. He, D. Zhao, *Environ. Sci. Technol.* **2007**, *41(17)*, 6216
59. L. B. Hoch, E. J. Mack, B. W. Hydutsky, J. M. Hershman, J. M. Skluzacek, T. E. Mallouk, *Environ. Sci. Technol.* **2008**, *42 (7)*, 2600.
60. Y. Liu, G. V. Lowry, *Environ. Sci. Technol.* **2006**, *40 (19)*, 6085.
61. S. R. Kanel, J.-M. Grenche, H. Choi, *Environ. Sci. Technol.* **2006**, *40 (6)*, 2045.
62. Y. Liu, T. Phenrat, G. V. Lowry, *Environ. Sci. Technol.* **2007**, *41 (22)*, 7881.
63. A. B. M. Giasuddin, S. R. Kanel, H. Choi, *Environ. Sci. Technol.* **2007**, *41 (6)*, 2022.
64. H. Song, E. R. Carraway, *Environ. Sci. Technol.* **2005**, *39 (16)*, 6237.
65. J. –H. Kim, P. G. Tratnyek, Y.-S. Chang, *Environ. Sci. Technol.* **2008**, *42 (11)*, 4106.
66. V. Sarathy, P. G. Tratnyek, J. T. Nurmi, D. R. Baer, J. E. Amonette, C. L. Chun, R. L. Penn, E. J. Reardon, *J. Phys. Chem. C* **2008**, *112 (7)*, 2286.

67. M. N. Nadagouda, R. S. Varma, *Green Chem.* **2006**, *8*, 516 .
68. P. Raveendran, J. Fu, S. L. Wallen, *J. Am. Chem. Soc* **2003**, *125*, 13940.
69. M. N. Nadagouda, R. S. Varma, *Green Chem.* **2007**, *9*, 632 .
70. R. R. Naik, S. J. Stringer, G. Agarwal, S. E. Jones, M. O. Stone, *Nat. Mater.* **2002**, *1*, 169 .
71. M. N. Nadagouda, R. S. Varma, *J. NanoMater.* **2008**, doi:1155/2008/782358.
72. P. Mukherjee, A. Ahmad, D. Mandal, S. Senapati, S. R. Sainkar, M. I. Khan, R. Parishcha, P. V. Ajaykumar, M. Alam, R. Kumar, M. Sastry, *Nano Lett.* **2001,** *1*, 515.
73. M. N. Nadagouda, R. S. Varma, *Green Chem.* **2008**, *10*, 859.
74. P. T. Anastas, J. C. Warner, *Green, Chemistry: Theory and Practice, Oxford University Press, Inc.* New York, **1998**.
75. M. N. Nadagouda, R. S. Varma, *Cryst. Growth Design* **2008**, *8*, 291.
76. M. N. Nadagouda, R. S. Varma, *Cryst. Growth Design* **2007**, *4*, 686.
77. M. N. Nadagouda, R. S. Varma, *Biomacromolecules* **2007**, *8*, 2762.
78. M. N. Nadagouda, R. S. Varma, *Macromol. Rapid Commun*. **2007**, *28*, 465.
79. M. N. Nadadgouda, V. Polshettiwar, R. S. Varma, *J. Mater. Chem.*, **2009**, *19*, 2026.
80. V. Polshettiwar, B. Baruwati, R. S. Varma, *Green Chem.* **2009**, *11*, 127.